nature methods

Article

https://doi.org/10.1038/s41592-025-02863-4

ESPRESSO: spatiotemporal omics based on organelle phenotyping

Received: 18 June 2024

Accepted: 17 September 2025

Published online: 03 November 2025

Check for updates

Lorenzo Scipioni[1,2,9] ✉, Giulia Tedeschi[1,2,9], Mariana X. Navarro[3], Yunlong Y. Jia[4,5], Songning Zhu[1], Lila P. Halbers[6], Melody Di Bona[7], Scott X. Atwood[4,5], Jennifer A. Prescher[3,6,8], Enrico Gratton[2] & Michelle A. Digman[2] ✉

Omics technologies such as genomics, transcriptomics, proteomics and metabolomics methods, have been instrumental in improving our understanding of complex biological systems by providing high-dimensional phenotypes of cell populations and single cells. Despite fast-paced advancements, these methods are limited in their ability to include a temporal dimension. Here, we introduce ESPRESSO (Environmental Sensor Phenotyping RElayed by Subcellular Structures and Organelles), a technique that provides single-cell, high-dimensional phenotyping resolved in space and time. ESPRESSO combines fluorescent labeling, advanced microscopy and image and data analysis methods to extract morphological and functional information from organelles at the single-cell level. We validate ESPRESSO's methodology and its application across numerous cellular systems for the analysis of cell type, stress response, differentiation and immune cell polarization. We show that ESPRESSO can correlate phenotype changes with gene expression, and demonstrate its applicability to 3D cultures, offering a path to improved spatially and temporally resolved biological exploration of cellular states.

Recent technological advancements have enabled the transition of omics technologies from homogenized bulk measurements to fine-grained single-cell and spatial analyses. Although informative, bulk approaches mask the inherent heterogeneity in cellular subpopulations. Single-cell techniques such as single-cell RNA sequencing (scRNA-seq) have overcome this limitation, and can identify distinct cell types and rare subpopulations, and provide insights into complex biological processes. However, scRNA-seq lacks spatial information, hindering our understanding of how individual cells[1–3] organize and interact. Spatial omics[4] represents the natural evolution of these technologies, and shows how phenotypes are spatially organized, as well as the communication networks between cells.

Despite these advancements, capture of the dynamic aspects of these interactions remains a significant challenge. Current omics techniques, while informative, often fall short in capturing the dynamic nature of biological transitions, particularly in metabolic shifts in which cells undergo rapid reprogramming of gene expression, protein activity and metabolic pathways. To unravel these complexities, time-resolved omics data with high temporal resolution are indispensable.

Indeed, transitions between observed phenotypes are just as important as their presence, given that numerous cellular processes leading to phenotypic changes occur over time, to regulate development (for example, differentiation), immune response (for example, macrophage polarization), or adaptation to external conditions (for

[1]Centre de Recherche en Cancérologie de Toulouse, Toulouse, France. [2]Department of Biomedical Engineering, Laboratory for Fluorescence Dynamics, University of California, Irvine, Irvine, CA, USA. [3]Department of Chemistry, University of California, Irvine, CA, USA. [4]Department of Developmental and Cell Biology, University of California, Irvine, CA, USA. [5]Department of Dermatology, University of California, Irvine, CA, USA. [6]Department of Pharmaceutical Sciences, University of California, Irvine, CA, USA. [7]Department of Radiation Oncology, Memorial Sloan Kettering Cancer Center, New York, NY, USA. [8]Department of Molecular Biology & Biochemistry, University of California, Irvine, CA, USA. [9]These authors contributed equally: Lorenzo Scipioni, Giulia Tedeschi. ✉e-mail: lorenzo.scipioni@inserm.fr; mdigman@uci.edu

example, stress response and metabolic switch). While the pursuit of spatiotemporal omics holds immense promise, adapting traditional approaches and achieving true spatiotemporal resolution presents significant challenges that must be addressed to achieve a deeper understanding of these biological processes.

We propose a paradigm shift to the viewing of organelles as a target for phenotyping. Extensive literature links organelle properties to specific cell states[5]. Organelle characteristics are tightly linked to cellular metabolic processes[6] and differentiation state[7], and they can provide information on the cell's bioenergetics[8]. They can identify the cellular response to specific stressors (for example, metabolic stress[9], mitochondrial fragmentation[10], mitophagy[11], lipid storage[12] and consumption[13]). In a process called organelle inheritance[14], daughter cells with different fates (for example, differentiation state) inherit organelles with different characteristics, hinting at the organelle network's importance in maintaining cellular homeostasis. Techniques such as the Cell Painting assay[15] leverage organelle properties using fluorescent dyes to target various components such as the nucleus, endoplasmic reticulum, mitochondria, cytoskeleton, Golgi apparatus and RNA, and can be used in drug discovery. Proteomics has also been applied in organelle-specific contexts with techniques such as nuclear proteomics[16], in which nuclear isolation followed by mass spectrometry analysis elucidates protein composition and interactions inside the nucleus. Overall, a clear link exists between the morphological and functional characteristics of the organelle network (hence, the "organelle landscape") and cell state.

Here, we developed ESPRESSO (Environmental Sensor Phenotyping REIayed by Subcellular Structures and Organelles), which provides high-dimensional phenotyping resolved in space and time. We assembled a panel of four organelle-specific, live-cell dyes with signal stable for at least 24 hours. Furthermore, we selected dyes that modify their fluorescence intensity based on the biophysical properties of their target organelle (for example, lysosomal acidity[17] and mitochondrial membrane potential[18]), and report on both morphological (for example, number, size, interaction and subcellular organization) and functional information from four organelles simultaneously. We imaged the labeled cells using hyperspectral imaging[19], a fluorescence microscopy technique that acquires the entire fluorescence emission spectrum pixel by pixel, to enable snapshot multicolor imaging. We then combined this labeling and imaging strategy with convolutional neural networks (CNNs), signal unmixing, image analysis and data analysis tools, to create the ESPRESSO framework. In the following sections we present ESPRESSO's methodology and its application across various cellular systems, showcasing its ability to discern different cell types, phenotype adaptation to stressor exposure, and cell lineage signature (keratinocyte differentiation, and macrophage polarization). We then show that ESPRESSO's phenotype changes correlate with gene expression and, as an example, we present its applicability to 3D triple-negative breast cancer (TNBC) spheroids in the analysis of their phenotype evolution during collagen invasion and response to various stressors. ESPRESSO represents a framework that offers high-dimensional phenotyping based on organelles, representing the first spatiotemporally resolved omics technique based on this approach.

Results

ESPRESSO workflow and cell type phenotyping

Development of a comprehensive method for spatiotemporal omics requires multiple techniques merged into a unified framework (Fig. 1a).

Organelle-specific, environment-sensitive dyes. First, we worked on defining a panel of four organelle-targeting, live-cell compatible fluorescent probes and optimized the staining protocol to achieve 24 hour continuous imaging with stable fluorescence signal and spectral signature in living cells (Supplementary Fig. 1). Importantly, prolonged incubation with the dyes, and imaging, do not significantly impact cell viability or cell stress (Supplementary Fig. 2). The emission spectra of the dyes panel, however, are highly overlapping (Supplementary Fig. 1) and preclude signal discrimination with conventional multicolor microscopy techniques (for example, multiple excitation and emission filter sets, Supplementary Fig. 3) that have the additional disadvantage of requiring sequential multicolor imaging, which would hinder the quantification of the relative position of different organelles inside the cells.

Hyperspectral imaging and phasor unmixing. To overcome this limitation we turned to hyperspectral imaging[20], a technique based on confocal microscopy that enables the simultaneous acquisition of the emission spectrum across the visible range in a pixel-wise manner. Once the hyperspectral image is acquired, we applied spectral phasor unmixing[21,22] to separate the signal of the individual probes, to achieve simultaneous imaging of the four organelle-targeting fluorophores in our panel, regardless of spectral or spatial overlapping. At this stage we confronted the challenge presented by the imaging speed. While a higher photon count improves the unmixing and quantification of the dyes' response, it also increases the phototoxicity to the sample.

Neural networks. To solve this conundrum we turned to CNNs, now ubiquitous in image analysis[23] due to their high performance and versatility. We leveraged that power by training a content-aware image restoration (CARE[24]) denoising CNN to increase the acquisition speed 16-fold while maintaining image quality and resolution (Supplementary Fig. 4). Furthermore, we added a cell-segmentation CNN (CellPose[25]) to our pipeline to achieve single-cell capability via cell segmentation.

Extraction of single-cell features. Once segmented, we addressed the extraction of the organelle features from each of the single cells. After unmixing, the images of the target organelles (lysosomes, mitochondria, lipid droplets and DNA) were analyzed morphologically using image correlation spectroscopy (ICS[26,27]), while intracellular organelle distribution was assessed using image cross-correlation spectroscopy (ICCS[28,29]). ICS and ICCS are well-established methods to investigate the number and size of subcellular structures[30–32] and their co-localization or distance inside the cell. Although all of the information about these important morphological features is indeed encoded in the ICS and ICCS functions, a model is traditionally applied to quantify them. This forces us to make assumptions about the type of model to apply to quantify the organelles under analysis. Aiming to construct ESPRESSO as a general framework, we bypassed modeling and fitting and we leveraged the entire ICS and ICCS functions, considering each bin of their rotational average as a morphological feature. A similar approach was taken when extracting functional information. Indeed, the fluorescence intensity of each of the selected organelle dyes is dependent on a defined property of the target organelle (acidity for lysosomes, membrane potential for mitochondria, fatty acids storage for lipid droplets and chromatin organization for DNA). Similarly to morphological features, we assessed functional features by computing the log-intensity distribution of each unmixed organelle image. Information about the heterogeneity in the function of individual organelles is encoded not only by descriptors of the distribution, but also by the distribution in its entirety, as described in detail in the Methods section. As a result, a collection of 3,328 features was obtained to report on morphology, intracellular organization and function, that can be carried over to the final step in our pipeline, which concerns the analysis of the organelle profiles.

Data analysis and clustering. Similarly to gene expression profiles in scRNA-seq, organelle properties are normalized, selected and reduced in dimensionality by PaCMAP (pairwise controlled manifold approximation projection)[33], to generate low-dimensional embeddings that encode the high-dimensional organelle properties of each cell. A

https://doi.org/10.1038/s41592-025-02863-4

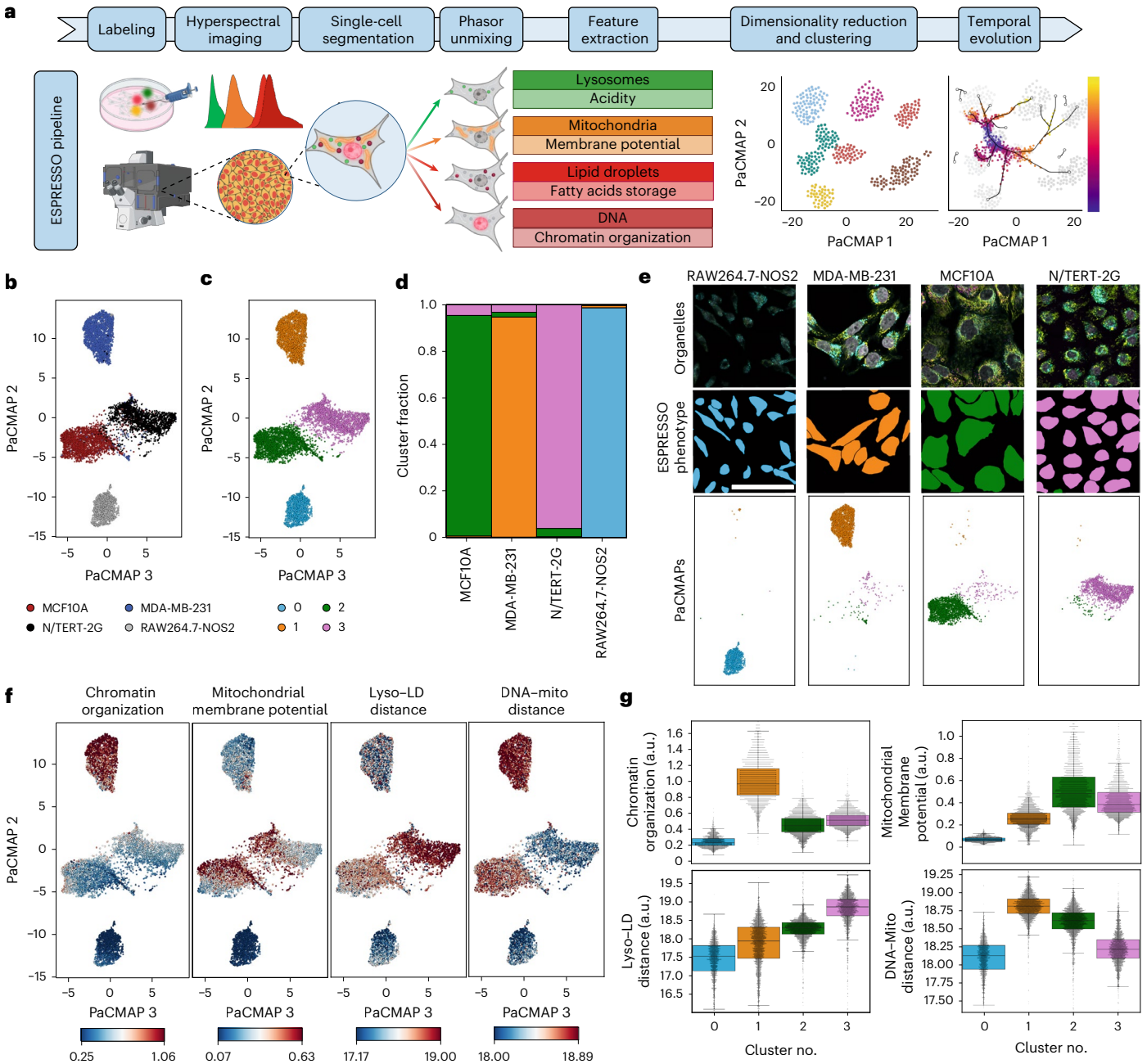

Fig. 1 | ESPRESSO workflow and organelle phenotypes of diverse cell lines. **a**, Schematic diagram of the ESPRESSO workflow (created in BioRender; Scipioni, L. (2025) https://BioRender.com/os92ls5, agreement: KR28GXNJR7). Cells are labeled with a panel of fluorescent dyes, followed by hyperspectral imaging. Organelle images are unmixed and their features are extracted and dimensionally reduced. **b**,**c**, ESPRESSO PaCMAP of 8,838 cells from four different cell lines (MCF10A, MDA-MB-231, N/TERT-2G and RAW264.7-NOS2) color-coded by cell line (**b**) and ESPRESSO phenotype (**c**). **d**, The stacked bar plot shows the cluster fraction for each ESPRESSO phenotype. **e**, Representative regions of interest showing the unmixed organelle images (top: white, DNA; yellow, mitochondria; cyan, lysosomes; magenta, lipid droplets), the cell masks color-coded by ESPRESSO phenotype (center) and corresponding ESPRESSO PaCMAPs (bottom). **f**, ESPRESSO PaCMAPs color-coded by representative organelle properties, calculated as the center of mass of the intensity distribution, cross- or auto-correlation curves, as described in the Methods section. **g**, Swarm plots and box-and-whiskers plots quantifying the properties shown in **f** for each cluster. The black central line in the box-and-whiskers plot denotes the median, the box extends between the upper and lower quartiles and the whiskers extend between the minimum and maximum values, excluding outliers. Data are derived from three biological replicates with one technical replicate each. Scale bar, 50 µm. LD, lipid droplet; Lyso, lysosome; Mito, mitochondria; a.u., arbitrary units.

Gaussian mixture model[34] clustering algorithm is then applied and the number of clusters is based on the minimization of the Davies–Bouldin index[35], as described in the Methods (Supplementary Figs. 5 and 6). We will refer to these clusters that identify cell states based on organelle properties, as ESPRESSO phenotypes.

Thanks to a combination of stable organelle-targeting dyes, simultaneous multicolor imaging and denoising, signal unmixing (Supplementary Fig. 7a), cell segmentation, image analysis and data analysis tools, we can obtain ESPRESSO phenotypes at the single-cell level and assess their evolution as a function of time for over 24 hours (for a detailed workflow, see Supplementary Fig. 7b), as we demonstrate by discriminating between different cell types (Fig. 1b). While bleedthrough signal between the SMCy5.5 and the SiR-DNA dyes can still be seen (Supplementary Fig. 4) due to their spectral proximity,

it does not have a marked effect on the quantification, given that we do not observe a systematic correlation between lipid droplets and chromatin features (Supplementary Fig. 8).

Proof-of-concept experiment. We analyzed four different cell lines using the ESPRESSO pipeline as described above. We plated MDA-MB-231 (TNBC), MCF10A (non-tumorigenic epithelial), N/TERT-2G[36] (immortalized keratinocytes) and RAW264.7-NOS2[37] (mouse macrophages expressing a *NOS2* gene expression reporter) cells in growth conditions and segmented a total of 8,838 cells for ESPRESSO phenotyping. Gaussian mixture model clustering easily identified (Fig. 1c,d) the cell type-specific phenotypes that can be used to quantify the characteristics of their organelle network. As an example, MDA-MB-231 cells are characterized by a higher chromatin compaction when compared with the other cells lines (Fig. 1e), which are instead characterized by either high mitochondrial membrane potential (MCF10A), high lysosome–lipid droplet distance (N/TERT-2G) or low chromatin organization and low mitochondrial membrane potential (RAW264.7-NOS2). Finally, ESPRESSO phenotyping, being based on microscopy imaging, is intrinsically spatially resolved. Cell masks can be color-coded based on the assigned ESPRESSO phenotype (Fig. 1f), morphological and functional characteristics can be quantified (Fig. 1g) and their changes can be followed and analyzed over extended periods of time. As an example of a time-resolved dataset, a cell synchronization experiment performed over the course of 24 hours is shown in Supplementary Figure 9

ESPRESSO phenotype response to stressor exposure

After establishing that ESPRESSO can discriminate between cell types, we moved on to studying the effect of stressor exposure. Stress response is the cellular response to changes in environmental conditions and involves a multifaceted reprogramming of cellular processes to adapt to and overcome new environments. As an example, hypoxia (oxygen deprivation) reduces the cell's ability to generate energy through aerobic respiration[38], leading to a signaling cascade that ultimately results in metabolic reprogramming towards a more anaerobic energy production. Understanding how different cell lines behave in response to different stressors can provide valuable insights into cellular resilience and has the potential for therapeutic interventions aimed at modulating stress responses in disease states. Here, we exposed MCF10A cells to chemicals that changed the environmental conditions towards hypoxia ($CoCl_2$; ref. 39), cholesterol inhibition (simvastatin[40]), autophagy inhibition (bafilomycin A1; ref. 41), mitochondrial stress (FCCP, carbonyl cyanide-p-trifluoromethoxyphenylhydrazone[42]) and chromatin compaction (anacardic acid[43]) or decompaction (trichostatin A[44]) for 24 hours and measured the resulting ESPRESSO phenotype. Our aim is to demonstrate that the wealth of information obtained by ESPRESSO phenotyping can not only detect stress responses, but can also distinguish between different types of stress. Indeed, we expected the different treatments to activate distinct cellular stress response pathways, leading to distinct phenotypes, as a result of the environmental changes we introduced. From the ESPRESSO PaCMAPs (Fig. 2a,b) and cluster allocations (Fig. 2c), we can identify a major group of cells (center) and two distinct smaller groups that we can associate with cells containing large lysosomes (bottom), and with cells containing compacted chromatin (top), as can be seen in Figure 2d,e, which reflects the intrinsic heterogeneity of the cell population in itself. As for the ESPRESSO phenotype response to our panel of stressors, we observed two high-order effects across these chemicals: they either altered the allocation of phenotypes that also exist in control conditions ($CoCl_2$ and simvastatin) or they introduced new, stress-specific phenotypes (for example, trichostatin A, bafilomycin A; Fig. 2f). However, for $CoCl_2$ and simvastatin, the result of the phenotype adaptation was different between these two chemicals, given that $CoCl_2$ favored phenotypes with high fatty acid storage (consistent with a hypoxic response[45,46]), while simvastatin generated higher mitochondrial membrane potential and lysosomal acidity (Fig. 2d,e), consistent with what is reported elsewhere for other cell types[47,48]. The other stressors tested, however, had a radically different effect on the MCF10A cell culture, effectively driving the change in organelle traits towards a specific, stress-dependent phenotype. In this, ESPRESSO provided the unique advantage of not only detecting the exposure to various stressors, but also elucidating the mechanism of action on the cell population and defining a unique fingerprint for different stressors in living cells.

ESPRESSO time-resolved phenotype evolution during keratinocyte differentiation

Moving from stationary analysis of cell states, we turned to two major cellular processes that are intrinsically time-resolved: cell differentiation and macrophage polarization.

Cell differentiation characterizes the development from single cells to complex living organisms, and it is a dynamic process that involves the reprogramming of gene expression profiles. Such reprogramming defines the boundaries of a cell's function, and it is a highly regulated process that has been shown to have repercussions for the organelle landscape in various cell types. In human skin, keratinocytes undergo a continuous process of differentiation that begins in the basal layer, the deepest of the layers in the epidermis. As they divide, newly formed keratinocytes undergo progressive differentiation as they approach the cornified layer, the outermost layer, where they ultimately reach their terminal differentiation state, culminating in regulated cell death[49]. In vitro, keratinocytes can be grown in low-calcium medium and their differentiation can be triggered by calcium supplementation. As shown in Figure 3a, we seeded keratinocytes in either control conditions or supplementation with 1.2 mM calcium to induce differentiation. We imaged them over the course of 22.5 hours at 30 minute intervals, collecting information on a total of 73,430 cells. ESPRESSO reports striking phenotype differences between keratinocytes in control (Fig. 3b) and calcium-switch (Fig. 3c) conditions, showing the emergence of four differentiation-specific ESPRESSO phenotypes. Moreover, we were also able to assess the phenotype's temporal evolution, by visualizing the difference between phenotypes that arise quickly and others that manifest at a later stage (Fig. 3d,e), suggesting heterogeneity in the differentiation response. Calcium-specific phenotypes are characterized by drastic morphological and functional changes in the organelle landscape (Fig. 3f), such as an increase in nuclear size and lysosomal acidity in specific calcium-induced differentiation cell states, consistent with trends seen during keratinocyte differentiation in vivo[50,51]. Interestingly, the phenotype temporal evolution is also accompanied by a large-scale spatial rearrangement. In fact, the cell culture is no longer composed of isolated cells (Supplementary Video 1), and keratinocytes tend to organize in patches (Fig. 3g and Supplementary Video 2), suggesting that cell–cell contacts are increased upon calcium-induced differentiation, and mimicking in vivo trends[52]. Given that the phenotype changes during keratinocyte differentiation occur across both space and time, this application showcases the power of ESPRESSO spatiotemporal omics not only to identify the presence of distinct phenotypes, but also to provide insights into their spatiotemporal evolution.

ESPRESSO phenotype evolution during macrophage M1 activation correlates with gene expression

We sought to understand whether ESPRESSO phenotypes can be correlated with gene expression and focused on the process of macrophage polarization. Macrophages[53] are immune cells that target pathogens as well as bacteria or debris. They are characterized by a process named polarization, triggered by an inflammatory response, that leads to the acquisition of two broad phenotypes: pro-inflammatory (or M1-polarized) and anti-inflammatory (or M2-polarized) macrophages[54]. M1 polarization can be achieved in vitro by exposing the cells to lipopolysaccharide (LPS), a component of the outer membrane

https://doi.org/10.1038/s41592-025-02863-4

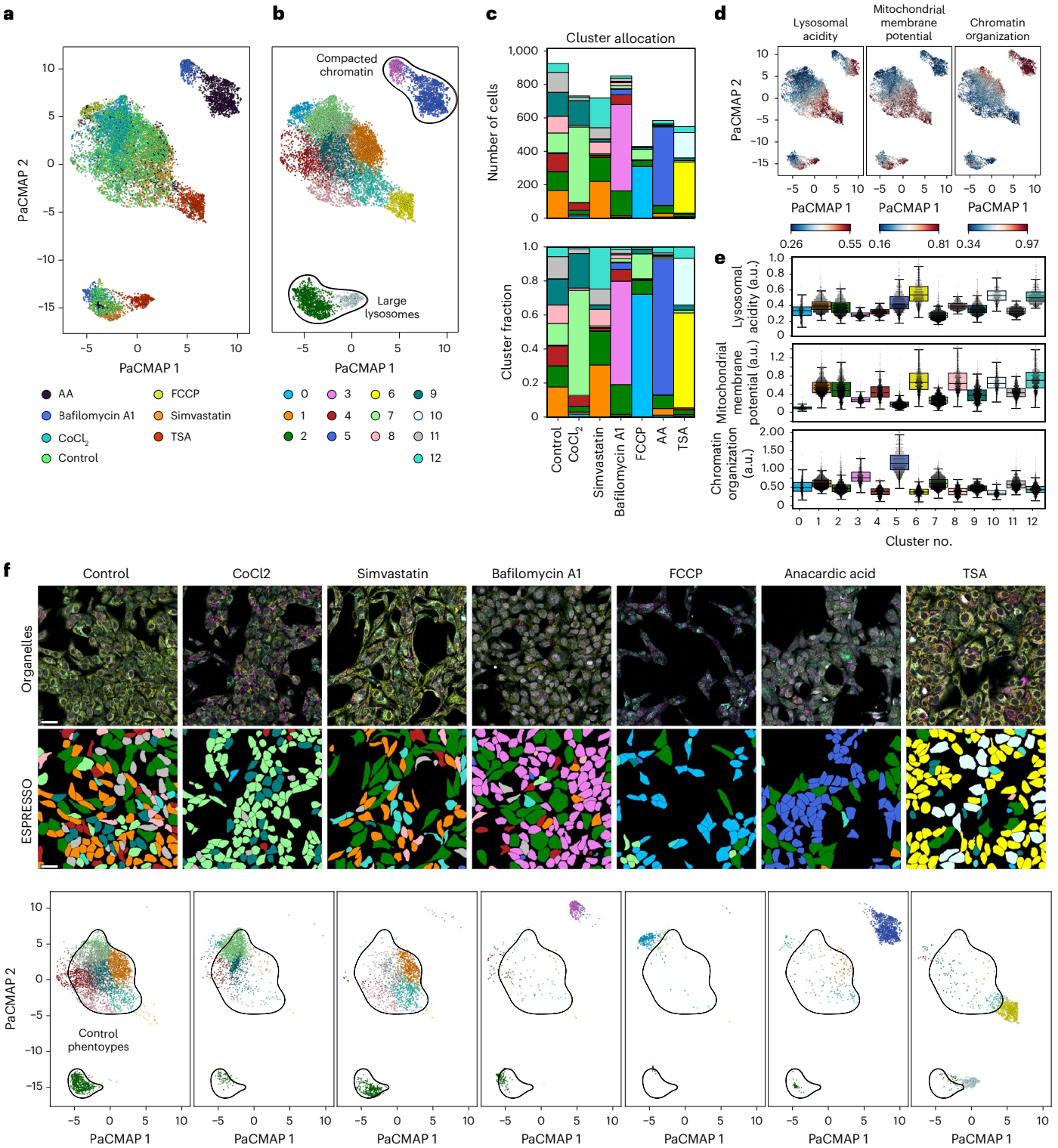

Fig. 2 | Differential ESPRESSO phenotype response to stressor exposure. **a**,**b**, ESPRESSO PaCMAP color-coded by cell treatment (**a**) and ESPRESSO phenotype (**b**). Regions highlighted in **b** correspond to phenotypes characterized by compacted chromatin (top) and large cells (bottom). **c**, Stacked bar plots highlighting the number of cells (top) and fraction (bottom) of ESPRESSO phenotypes arranged by cell treatment. **d**,**e**, ESPRESSO PaCMAPs color-coded by representative organelle properties (**d**) and corresponding swarm plots and box-and-whiskers plots (**e**). The black central line in the box-and-whiskers plot denotes the median, the box extends between the upper and lower quartiles and the whiskers extend between the minimum and maximum values, excluding outliers. Data are derived from three biological replicates with three technical replicates each. Organelle properties are calculated as the center of mass of the intensity distribution, cross- or auto-correlation curves, as described in the Methods section. a.u., arbitrary units. **f**, Representative regions of interest showing the unmixed organelle images (top: white, DNA; yellow, mitochondria; cyan, lysosomes; magenta, lipid droplets), the cell masks color-coded by ESPRESSO phenotype (middle), and the corresponding ESPRESSO PaCMAPs (bottom, regions highlight phenotypes present in control conditions). Scale bars, 50 µm. AA, anacardic acid; FCCP, carbonyl cyanide-p-trifluoromethoxyphenylhydrazone; LD, lipid droplet; Mito, mitochondria; TSA, trichostatin A.

https://doi.org/10.1038/s41592-025-02863-4

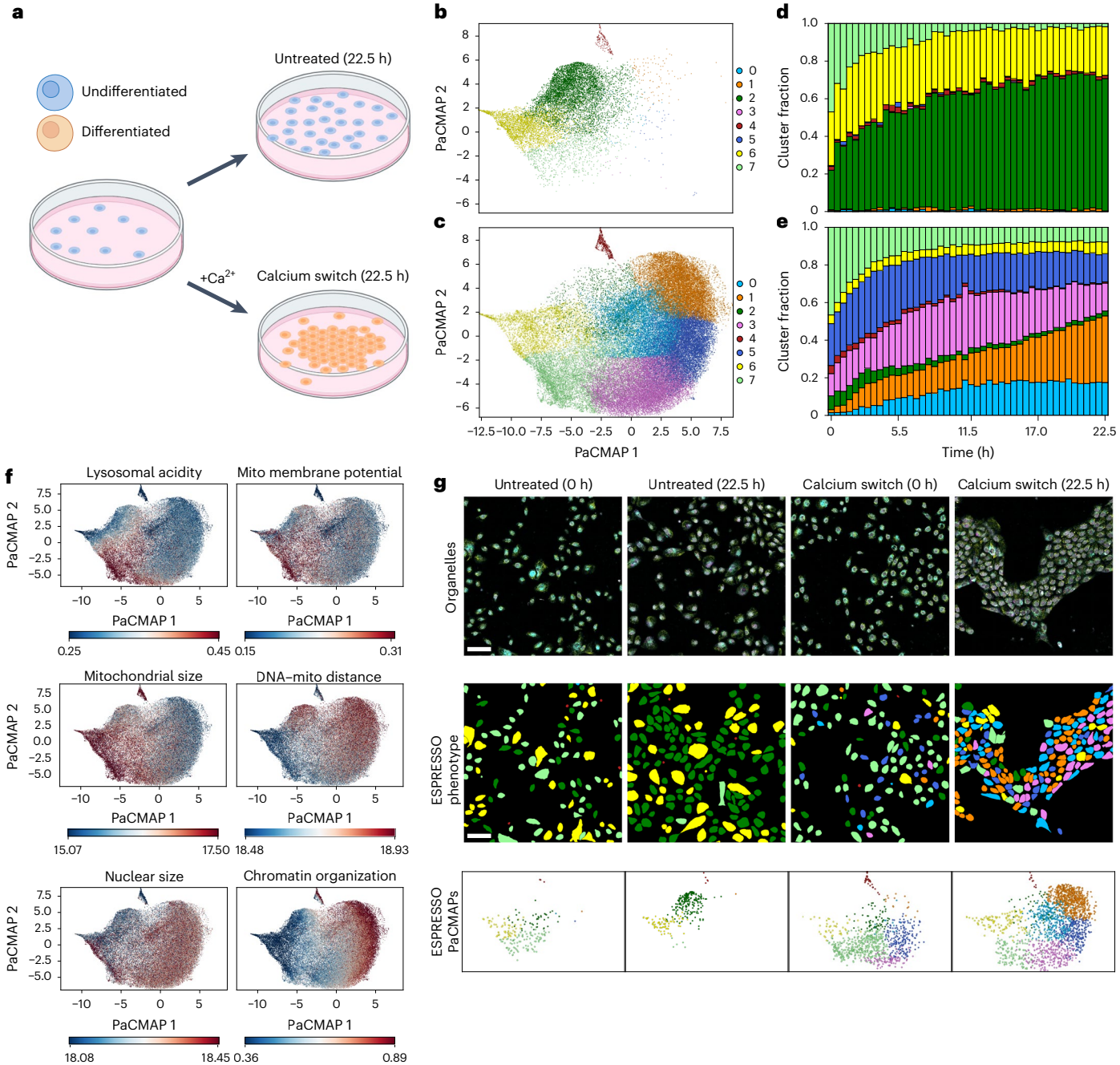

Fig. 3 | ESPRESSO phenotype evolution during keratinocyte differentiation. **a**, Schematic diagram of the experimental workflow (created in BioRender; Scipioni, L. (2025) https://BioRender.com/os92ls5, agreement: AI28GXNJU7). N/TERT-2G keratinocytes are plated and imaged for 22.5 h in growth conditions (top) or in medium supplemented with 1.2 mM Ca^{2+} to induce differentiation via calcium switch. **b**,**c**, ESPRESSO PaCMAPs of 73,430 cells in untreated (**b**) and calcium-switch (**c**) conditions, color-coded according to ESPRESSO phenotype. **d**,**e**, Stacked bar plots showing the cluster fraction as a function of time for keratinocytes in untreated (**d**) and calcium-switch (**e**) conditions. **f**, ESPRESSO PaCMAPs color-coded by representative organelle properties, calculated as the center of mass of the intensity distribution, cross- or auto-correlation curves, as described in the Methods section. **g**, Representative regions of interest showing the unmixed organelle images (top: white, DNA; yellow, mitochondria; cyan, lysosomes; magenta, lipid droplets), the cell masks color-coded by ESPRESSO phenotype (middle), and the corresponding ESPRESSO PaCMAPs (bottom). Scale bars, 100 µm. Mito, mitochondria. Data are derived from three biological replicates with three technical replicates each.

of Gram-negative bacteria. LPS is recognized as an inflammatory agent by macrophages, initiating M1 polarization as a result. M1 polarization is characterized by overexpression of numerous cytokines and chemokines, together with enzymes and other proteins that prepare the cell to counteract a potential infection. Of these, iNOS (inducible nitric oxide synthase) plays a crucial role in the production of nitric oxide (NO) and its expression is regulated by *NOS2* (ref. 55). Here, we used an immortalized mouse macrophage cell line (RAW264.7-NOS2[37]) stably transduced with a gene expression reporter for *NOS2*. Upon *NOS2* expression, the cell line also expresses CeNL, a bioluminescent reporter comprising a fluorescent protein (mTurquoise2): the intensity of the fluorescent reporter correlates directly with *NOS2* expression. For this experiment we seeded RAW264.7-NOS2 macrophages in growth conditions and in the presence of LPS (Fig. 4a) and imaged them for 24 h in 30 minute intervals. Importantly, we simultaneously monitored the ESPRESSO phenotype (Fig. 4b,c) as well as mTurquoise2 fluorescence

https://doi.org/10.1038/s41592-025-02863-4

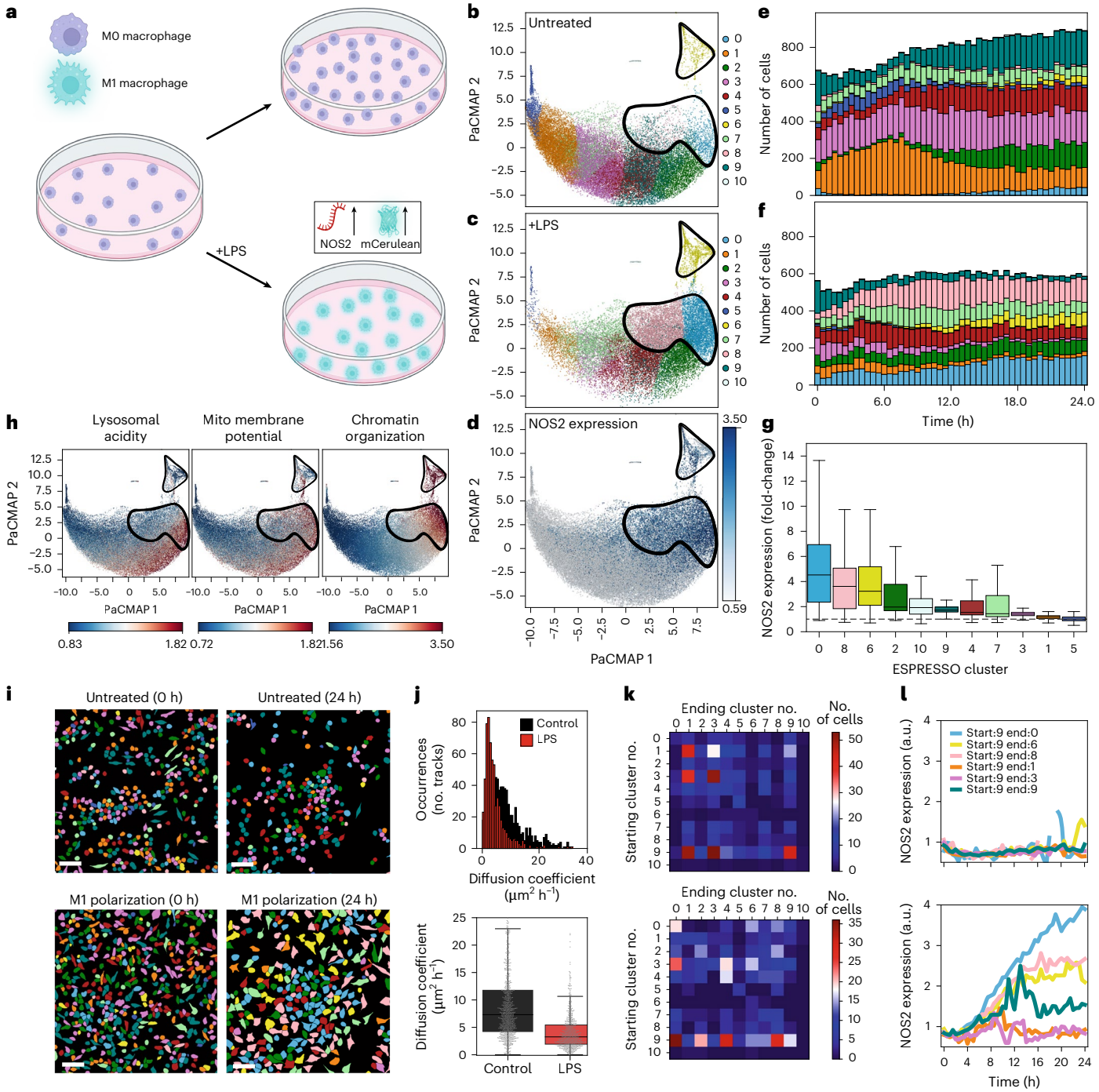

Fig. 4 | Correlation of ESPRESSO phenotype evolution during macrophage M1 polarization with gene expression. a, Schematic diagram of the experimental workflow (created in BioRender; Scipioni, L. (2025) https://BioRender.com/os92ls5, agreement: DX28GXNJW9). RAW 264.7 macrophages transduced with a NOS2-mCerulean gene expression reporter are plated and imaged for 24 h in growth conditions (top) or in medium supplemented with LPS. **b**,**c**, ESPRESSO PaCMAPs of 67,381 cells in untreated (**b**) and M1 polarization (**c**) conditions, color-coded according to the ESPRESSO phenotypes. **d**, ESPRESSO PaCMAP color-coded according to *NOS2* gene expression, calculated as the center of mass of the mCerulean intensity distribution. **e**,**f**, Stacked bar plot showing the number of cells per cluster as a function of time for macrophages in untreated (**e**) and M1 polarization (**f**) conditions. **g**, Box-and-whiskers plot showing the distribution of *NOS2* expression per cluster as the fold-change relative to the cluster with the least expression. The dashed horizontal line at 1 serves as a visual guide. **h**, ESPRESSO PaCMAPs color-coded by representative organelle properties, calculated as the center of mass of the intensity distribution as described in the Methods section. **i**, Representative regions of interest at 0 h and 24 h for Control and LPS-treated cells, showing the cell masks color-coded by ESPRESSO phenotype. **j**, Histogram (top) and box-and-whiskers and swarm plots (bottom) of the diffusion coefficient obtained by analyzing tracks from 837 control and 636 LPS-treated cells. Gray dots in **j** (bottom) denote the calculated diffusion coefficient from individual tracks. **k**, Cell state transition matrices from control (top) and LPS-treated (bottom) cells, representing the number of cells that belonged to a certain cluster (starting cluster no.) in the first 2 h of the experiment and transitioned to another (ending cluster no.) at the end of the track. **l**, Curves representing *NOS2* expression level for control (top) and LPS-treated (bottom) cells as a function of time. In box-and-whiskers plots, the central black line identifies the median while the extension of the box identifies the upper and lower quartiles, and the whiskers extend to the minimum and maximum values, excluding outliers. Scale bars, 50 μm. Mito, mitochondria. Data in **g** and **j** are derived from one biological replicate with three technical replicates each.

intensity (Fig. 4d), to enable the concurrent detection of organelle properties and *NOS2* gene expression. We identified three ESPRESSO phenotypes (clusters 0, 6 and 8) exclusively present or enriched after 24 h of LPS exposure (Fig. 4e,f). These ESPRESSO phenotypes are characterized by chromatin reorganization and an increase in lysosomal acidity and mitochondrial membrane potential, effects also reported in the literature[37]. Importantly, we quantify the gene reporter fluorescence intensity levels and found all three phenotypes to significantly upregulate *NOS2* expression (Fig. 4d,g), providing a direct link between gene expression and the organelle reorganization (Fig. 4h). Expanding our analysis further, we performed cell tracking on our dataset (example of images color-coded by ESPRESSO phenotype shown in Fig. 4i), obtaining tracks from 837 control and 636 LPS-treated cells, to quantify an overall decrease in cell migration (Fig. 4j) with LPS treatment. Leveraging the possibility to continuously monitor individual cells, we constructed cell state transition matrices (Fig. 4k) that can characterize the most common cell state transitions (red squares). Notably, we can observe a profound change in these transitions between control and LPS-treated cells. In particular, cell state transition from cluster 9 in control conditions veers towards clusters 1, 3 and 9 itself, while LPS treatment increases the weight toward M1-specific ESPRESSO clusters (0, 6 and 8). Finally, as expected, we can observe that the transition from cluster 9 to M1-specific ESPRESSO clusters results in a significant increase in *NOS2* expression (Fig. 4l), which is not the case if we consider the cell state transitions that are common in control conditions (1, 3 and 9), that maintain a lower expression of *NOS2* on par with values measured in control conditions. This shows that ESPRESSO can not only identify phenotypes that correlate with *NOS2* expression, but can also identify the panorama of cell state transitions occurring between these phenotypes, and thereby highlighting the ones that will eventually result (or not) in an increase of expression of the target gene.

Keratinocyte differentiation with ESPRESSO and single-cell RNA sequencing

ESPRESSO extracts high-dimensional morphological and functional information from a number of organelle markers. Can this information be related to other high-dimensional phenotyping methods, in particular transcriptomics? To answer this question we performed an experiment (Fig. 5a) in which we analyzed a culture of N/TERT-2G keratinocytes in control conditions or exposure to 1.2 mM calcium for 24 hours, using ESPRESSO. After imaging we detached the cells, performed scRNA-seq (Supplementary Fig. 10), and compared the scRNA-seq results with those of ESPRESSO analysis (Supplementary Fig. 11).

There are notable similarities and differences between the two techniques. In terms of dimensionality, we recover similar values in terms of number of cells (scRNA-seq, 11,907; ESPRESSO, 15,414), data dimensionality (scRNA-seq, 6,669 median number of genes per cell; ESPRESSO, 3,328 features per cell) and number of features used for dimensionality reduction (scRNA-seq, 2,000; ESPRESSO, 555). The resulting phenotype maps also appear similar, in that both methods recovered clusters that were either shared between the two samples or were specific to calcium differentiation (Fig. 5b–e). As a result, we divided both datasets into two macro-phenotypes: shared and calcium specific (Fig. 5f,g). We then proceeded to evaluate differences in enrichment of specific gene sets that could correlate with ESPRESSO (Fig. 5h,i), finding a positive correlation between an increase in the number of, and fatty acid storage by, lipid droplets in ESPRESSO, and the upregulation of fatty acid metabolism and adipogenesis in scRNA-seq. Furthermore, we show a marked increase in chromatin organization (with ESPRESSO) that correlated with a decrease in stemness (with scRNA-seq, quantified by CytoTRACE), while we observe a minimal increase in the size of nuclear features (ESPRESSO) and a small decrease in chromatin regulation (scRNA-seq). Similarities between the two techniques extended to the mitochondrial features, while the lysosomal features were found to be contradictory, with scRNA-seq expecting an increase in lysosomal acidification while ESPRESSO reports a decrease in lysosomal acidity (Supplementary Fig. 12). Among the differences, ESPRESSO picked up a rare cluster of cells (~0.1 % of the cell population) characterized by larger cellular area and unique morphological properties for which we do not see the correspondence in scRNA-seq. Furthermore, while scRNA-seq suggests an increase in lysosomal acidity based on lysosomal gene sets enrichment (Supplementary Fig. 12a), ESPRESSO detects a decrease in lysosomal acidity with unchanged lysosomal size (Supplementary Fig. 12b).

While similarity between the two techniques is important for validation and interpretability, the differences highlight the importance of combining upstream (gene expression by scRNA-seq) and downstream (organelle features by ESPRESSO) phenotyping methods. In addition to phenotype analysis, and differently from scRNA-seq, ESPRESSO also enables spatial analysis (Supplementary Fig. 13). Analysis of the inter-cluster neighborhood enrichment score showed a marked increase in association between the calcium-specific phenotypes, which tend to localize close to each other, and a marked decrease in association between the calcium-specific and the shared phenotypes, which instead tend to localize away from each other after calcium-induced differentiation. Overall, we have demonstrated the compatibility between ESPRESSO and scRNA-seq. The synergy between these two techniques will enhance the understanding of cellular phenotypes, providing high-dimensional, interpretable gene expression profiles (scRNA-seq) together with spatiotemporal context (ESPRESSO).

Phenotype response in 3D cultures: tumor spheroid invasion and response to stressors

So far, we have applied ESPRESSO phenotyping to both static and longitudinal analysis of cell types, stressor exposure, differentiation, and polarization in 2D cell cultures. Many biological systems, however, are not well recapitulated in vitro in 2D cultures, and instead require complex 3D systems[56–58]. An example of these systems is TNBC, a highly aggressive class of breast cancer particularly resistant to chemotherapy due to the loss of three major chemotherapy targets (estrogen receptor, progesterone receptor and HER2[59]). In breast cancer studies, tumor spheroids and organoids have been shown to better recapitulate the cell types found in vivo, making them an invaluable tool in the battle against cancer[60,61]. We sought to demonstrate that ESPRESSO can be applied longitudinally to complex 3D cultures and can be used to assess phenotype-specific responses to stressors in 3D tumor spheroids. To this aim, we generated tumor spheroids from TNBC cells (MDA-MB-231) and subsequently embedded them in a collagen matrix, similarly to our previous work[20,62,63]. Over time, cells at the surface of the spheroids undergo a metabolic switch and begin invading the collagen matrix, an event occurring at approximately 12–16 hours after embedding (Fig. 6a). To capture the phenotype evolution of single cells in TNBC spheroids, we performed a 16 hour volumetric time lapse from 9 to 25 hours after embedding (Fig. 6b–e). We observed the increase in allocation of two clusters (0 and 3 in Fig. 6d) during collagen invasion. We postulate that these phenotypes are the collagen-invading phenotypes, as also supported by the fact that cells in these clusters localize further from the spheroid center (Fig. 6c). This analysis can precisely identify the characteristics of collagen-invading phenotypes, thereby providing tools to target them specifically. It is worth noting that ESPRESSO analysis is limited to collagen-invading cells and the superficial layers of the spheroids, and does not extend to the deeper layers. This is due to the compact nature of TNBC tumor spheroids, which poses an obstacle to both the diffusion of the dyes and the penetration of the illumination laser, and which should be evaluated on a case-by-case basis when applying ESPRESSO to 3D samples.

A common parameter used to assess the viability of a spheroid culture is the size (or number of cells) as a function of time or concentration of a specific treatment[64]. Nonetheless, for a more comprehensive evaluation of treatment response, it is essential to consider the nature

https://doi.org/10.1038/s41592-025-02863-4

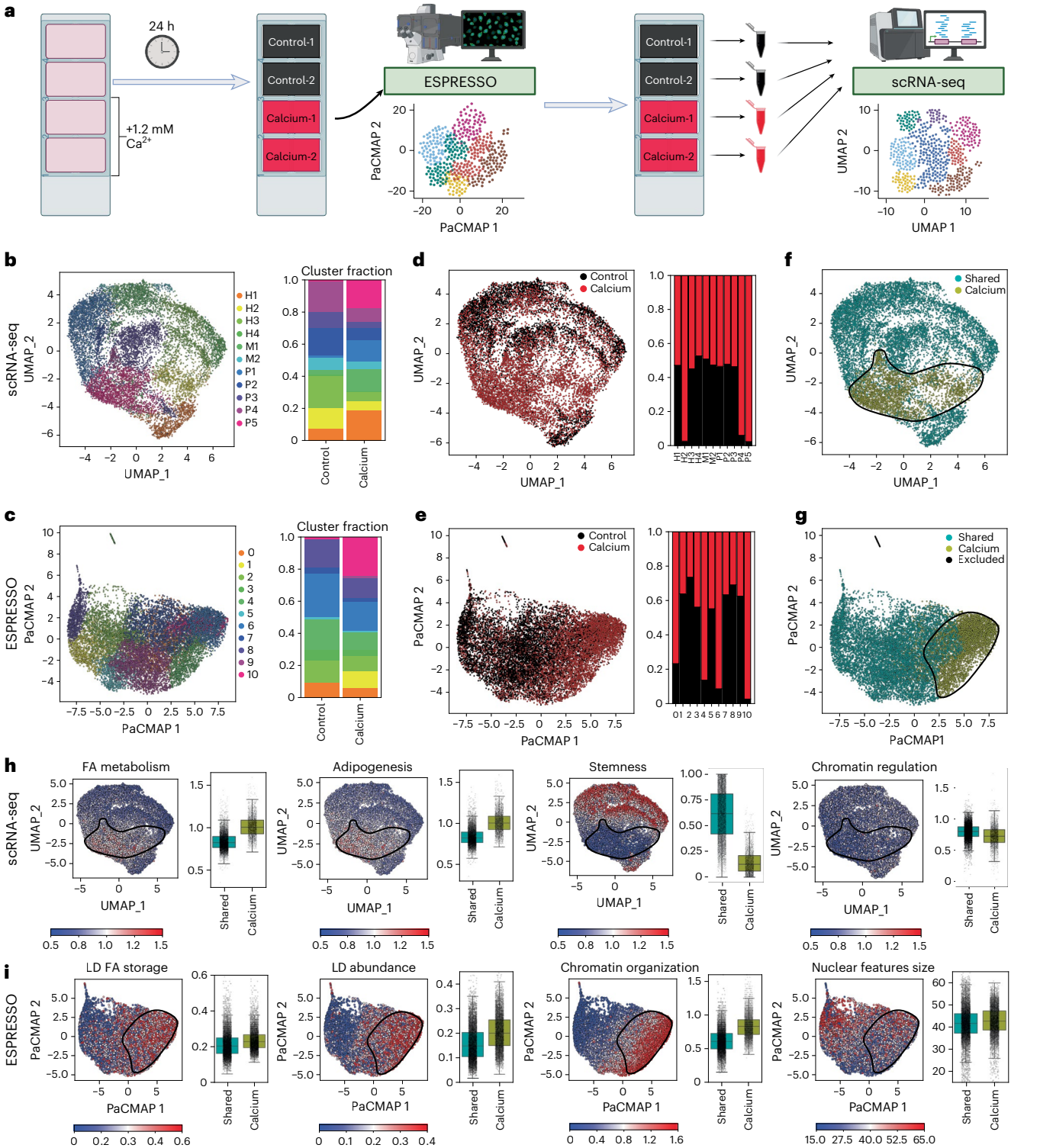

Fig. 5 | ESPRESSO and scRNA-seq: multiomics phenotype characterization of keratinocyte differentiation. a, Schematic diagram of the experimental workflow (created in BioRender; Scipioni, L. (2025) https://BioRender.com/os92ls5, agreement: CW28GXNJZ8). N/TERT-2G keratinocytes were plated in 4-well plates and cultured in growth medium (Control-1 and Control-2) or in 1.2 mM Ca^{2+} (Calcium-1 and Calcium-2) for 24 h. All samples were imaged for ESPRESSO phenotyping, and then the samples were successively detached and sequenced via scRNA-seq. **b**–**g**, Single-cell analysis by scRNA-seq (**b**,**d**,**f**) and ESPRESSO (**c**,**e**,**g**), showing low-dimensional embeddings color-coded by cluster (**b**,**c**, left) or experimental condition (**d**,**e**, left), along with bar plots showing the cluster fraction per condition (**b**,**c**, right) or the fraction of cells of different condition per cluster (**d**,**e**, right). Given that both methods output a number of clusters that are calcium specific (red bars in **d** and **e**, right) and others that are shared between the two conditions, we have defined two macro-phenotypes: Calcium and Shared, color-coded yellow and cyan, respectively, in the low-dimensional embeddings in **f** and **g**. **h**,**i**, Heatmaps for gene sets enrichment obtained by scRNA-seq (**h**) or organelle features obtained by ESPRESSO (**i**) and the corresponding boxplot for the two macro-phenotypes, with black dots representing values for individual cells. The highlighted regions represent the areas corresponding to the Calcium macro-phenotype. Data are derived from one biological replicate with two technical replicates each. The black central line in the box-and-whiskers plot denotes the median, the box extends between the upper and lower quartiles and the whiskers extend between the minimum and maximum values, excluding outliers. FA, fatty acid; LD, lipid droplet.

https://doi.org/10.1038/s41592-025-02863-4

of the targeted cells. To understand which cells are more susceptible to specific treatments, we sought to analyze how each chemical affects the phenotype composition of the spheroid. Indeed, we will show that ESPRESSO can identify whether or not the collagen-invading phenotypes in the 3D TNBC organoids are targeted by an external treatment (Fig. 6f). We exposed the spheroids to $CoCl_2$ and simvastatin for 72 h and mapped their ESPRESSO phenotype (Fig. 6g,h). We used two different concentrations of $CoCl_2$, 100 µM or 300 µM, because

Fig. 6 | ESPRESSO in 3D tumor spheroids: phenotype evolution and response to stressors. a, Schematic diagram of the experimental workflow for the phenotype evolution experiment. MDA-MB-231 spheroids are generated, embedded in collagen and imaged for 16 h (9–25 h after embedding) in growth conditions. **b**, ESPRESSO PaCMAP of 375,964 cells obtained from three spheroids and color-coded according to ESPRESSO phenotype. **c**, ESPRESSO PaCMAPs color-coded by representative organelle properties, calculated as the center of mass of the intensity distribution or auto-correlation curves, as described in the Methods section. **d**, Stacked bar plot showing the number of cells (top) and cluster fraction (bottom) as a function of time. **e**, Representative images and PaCMAPs showing the cell masks color-coded by ESPRESSO phenotype (top) and corresponding ESPRESSO PaCMAPs (bottom) for a tumor spheroid at 9 (left) and 25 h (right) after embedding. **f**, Schematic diagram of the experimental workflow for the stressor experiment. MDA-MB-231 spheroids are generated, embedded in collagen and imaged after 72 h in growth conditions (control) or in culture medium containing 100 μM $CoCl_2$, 300 μM $CoCl_2$ or simvastatin (SIM). **g**, ESPRESSO PaCMAP of 97,150 cells obtained from four spheroids per condition and color-coded according to ESPRESSO phenotype. **h**, ESPRESSO PaCMAPs color-coded by representative organelle properties, calculated as the center of mass of the intensity distribution as described in the Methods section. **i**, Number of segmented cells per spheroid for the different conditions. Statistical significance was calculated using the Student's t-test (two-sided) with Bonferroni correction. NS, $P > 0.05$; $^{**}P < 0.01$ and >0.001; $^{***}P < 0.001$ and >0.0001. *P* values for all comparisons are as follows: control versus $CoCl_2$ [100 μM], 1.000; $CoCl_2$ [100 μM] versus $CoCl_2$ [300 μM], 1.945×10^{-3}; $CoCl_2$ [300 μM] versus SIM, 1.384×10^{-1}; control versus $CoCl_2$ [300 μM], 1.293×10^{-3}; $CoCl_2$ [100 μM] versus SIM, 4.750×10^{-4}; control versus SIM, 1.819×10^{-4}. The black central line in the box-and-whiskers plot denotes the median, the box extends between the upper and lower quartiles and the whiskers extend between the minimum and maximum values, excluding outliers. **j**, Stacked bar plot showing the number of cells (top) and cluster fraction (bottom). **k**,**l**, Representative images and PaCMAPs showing the cell masks color-coded by ESPRESSO phenotype (top) and corresponding ESPRESSO PaCMAPs (bottom) for representative tumor spheroids for control and $CoCl_2$ [100 μM] (**k**), and $CoCl_2$ [300 μM] and simvastatin (**l**). Scale bars: **e**,**k**, 250 μm. LD, lipid droplet; Mito, mitochondria. Data are derived from one biological replicate with four technical replicates each. **a** and **f** created in BioRender: Scipioni, L. (2025) https://BioRender.com/os92ls5, agreements: AY28GXNK0R and PK28GXNK3K.

they are reported to have different effects on spheroid growth[65], as reflected by the cell number per spheroid (Fig. 6i) being unaffected for 100 μM and dramatically decreasing for 300 μM $CoCl_2$. Additionally, we considered simvastatin at a concentration causing a similar reduction in the spheroid cell number[66]. First, we identified the collagen-invading phenotypes (2, 5 and 8) as the phenotypes that characterize cells that have migrated further from the center of the spheroid. For each condition, we report on the cluster allocation for the ESPRESSO phenotypes (Fig. 6j). Then, we note that $CoCl_2$ has an effect on the spheroids (Fig. 6k), while not affecting the number of cells per spheroid. This effect is mostly localized to cells closer to the surface of the spheroid, where cells undergo a major phenotype change towards highly acidic lysosomes, while the collagen-invading phenotypes are not affected. Indeed, even at a cytotoxic concentration of 300 μM, we can see a major phenotype change on the surface of the spheroid, while the collagen-invading phenotypes are still present in a high percentage, suggesting a resistance of collagen-invading phenotypes to hypoxic conditions. In contrast, while also reducing the number of cells per spheroid, simvastatin exposure results in a massive population shift (Fig. 6l) towards a unique phenotype (cluster 4) and, more importantly, in a drastic reduction of the collagen-invading phenotypes. While the beneficial effect of simvastatin in the treatment of breast cancer has been investigated in the past and recently, with ESPRESSO we can show that the mechanism underlying this outcome relies on the ability of simvastatin to target collagen-invading TNBC phenotypes in vitro, introducing a unique phenotype that is underrepresented in both control and hypoxic conditions.

Discussion

While current omics techniques offer valuable snapshots of cellular states, they can fail to capture the dynamic nature of biological processes. This is particularly true for metabolic transitions, in which cells undergo rapid reprogramming of gene expression, protein activity and metabolite usage. To fully understand these transitions and their role in health and disease, time-resolved omics data with high temporal resolution are crucial. Although methods that enable time-resolved phenotyping exist, they are not often limited to particular processes[67], require heavy training[68,69], rely on genetic manipulation[67] and/or are not applicable to 3D models[68,70]. Indeed, a high-dimensional phenotyping technique that is applicable at the single-cell level, time-resolved and that does not require genetic manipulation would be game-changing in omics technology, with important repercussions in biology and medicine. Such data would enable researchers to track the step-by-step changes that occur during transition, elucidating key regulatory points and potential therapeutic targets. The development of faster, more sensitive omics techniques is therefore essential to unlock the secrets of these dynamic metabolic shifts. However, despite the organelle landscape's importance, consistent, broadly applicable methods for reliably extracting morphological and functional information from organelles, especially in a time-resolved manner, are lacking. This stems from several technical and technological barriers: the lack of stable, organelle-specific fluorescent dyes suitable for live-cell imaging hinders longitudinal studies; the limited number of snapshot multicolor technologies results in long integration times and high phototoxicity; and existing profiling methods are typically use-specific and difficult to generalize to other biological samples.

This work introduces ESPRESSO (Environmental Sensor Phenotyping RElayed by Subcellular Structures and Organelles), a spatiotemporally resolved, high-dimensional, single-cell technique aimed at improving our understanding of the organelle landscape in health and disease. As omics technologies have progressed from bulk, to single-cell, to spatial analyses, the need to access dynamic interactions in cellular systems has become increasingly important. ESPRESSO offers insights into cellular plasticity and paves the way for new discoveries in biology and potential therapeutic interventions in various disease states. A number of technical limitations remain, notably related to dye penetration in tissues. Indeed, depending on the accessibility of the 3D system, some dyes will need to be excluded or designed ad hoc. Furthermore, we are currently targeting only four organelles. While important for their implications in metabolism and other physiological cellular processing, increasing the number of targets could provide important insights into other processes, such as migration/adhesion and protein synthesis and processing, for example. Future directions for ESPRESSO development include overcoming the aforementioned limitations, while exploring a functional link between organelle features and protein and gene expression, by leveraging spatial proteomics and transcriptomics, respectively. ESPRESSO provides the research community with a powerful phenotyping tool to explore the intricate workings of complex cellular systems with detail and precision.

Online content

Any methods, additional references, Nature Portfolio reporting summaries, source data, extended data, supplementary information, acknowledgements, peer review information; details of author contributions and competing interests; and statements of data and code availability are available at https://doi.org/10.1038/s41592-025-02863-4.

References

1. Wang, Z., Gerstein, M. & Snyder, M. RNA-Seq: a revolutionary tool for transcriptomics. *Nat. Rev. Genet.* **10**, 57–63 (2009).

2. Cui, M., Cheng, C. & Zhang, L. High-throughput proteomics: a methodological mini-review. *Lab. Invest.* **102**, 1170–1181 (2022).
3. Johnson, C. H., Ivanisevic, J. & Siuzdak, G. Metabolomics: beyond biomarkers and towards mechanisms. *Nat. Rev. Mol. Cell Biol.* **17**, 451–459 (2016).
4. Lewis, S. M. et al. Spatial omics and multiplexed imaging to explore cancer biology. *Nat. Methods* **18**, 997–1012 (2021).
5. Valm, A. M. et al. Applying systems-level spectral imaging and analysis to reveal the organelle interactome. *Nature* **546**, 162–167 (2017).
6. Jain, A. & Zoncu, R. Organelle transporters and inter-organelle communication as drivers of metabolic regulation and cellular homeostasis. *Mol. Metab.* **60**, 101481 (2022).
7. Kim, Y. et al. Characterizing organelles in live stem cells using label-free optical diffraction tomography. *Mol. Cells* **44**, 851–860 (2021).
8. Ahlqvist, K. J., Suomalainen, A. & Hämäläinen, R. H. Stem cells, mitochondria and aging. *Biochim. Biophys. Acta* **1847**, 1380–1386 (2015).
9. Jarc, E. & Petan, T. Lipid droplets and the management of cellular stress. *Yale J. Biol. Med.* **92**, 435–452 (2019).
10. Frank, M. et al. Mitophagy is triggered by mild oxidative stress in a mitochondrial fission dependent manner. *Biochim. Biophys. Acta* **1823**, 2297–2310 (2012).
11. Mukhopadhyay, S. et al. Serum starvation induces anti-apoptotic cIAP1 to promote mitophagy through ubiquitination. *Biochem. Biophys. Res. Commun.* **479**, 940–946 (2016).
12. Cruz, A. L. S., Barreto, E. A., Fazolini, N. P. B., Viola, J. P. B. & Bozza, P. T. Lipid droplets: platforms with multiple functions in cancer hallmarks. *Cell Death Dis.* **11**, 105 (2020).
13. Rambold, A. S., Cohen, S. & Lippincott-Schwartz, J. Fatty acid trafficking in starved cells: regulation by lipid droplet lipolysis, autophagy, and mitochondrial fusion dynamics. *Dev. Cell* **32**, 678–692 (2015).
14. Loeffler, D. et al. Asymmetric organelle inheritance predicts human blood stem cell fate. *Blood* **139**, 2011–2023 (2022).
15. Bray, M. A. et al. Cell Painting, a high-content image-based assay for morphological profiling using multiplexed fluorescent dyes. *Nat. Protoc.* **11**, 1757–1774 (2016).
16. Novikova, S. et al. Nuclear proteomics of induced leukemia cell differentiation. *Cells* **11**, 3221 (2022).
17. Chikte, S., Panchal, N. & Warnes, G. Use of LysoTracker dyes: a flow cytometric study of autophagy. *Cytometry A* **85**, 169–178 (2014).
18. Scaduto, R. C. & Grotyohann, L. W. Measurement of mitochondrial membrane potential using fluorescent rhodamine derivatives. *Biophys. J.* **76**, 469–477 (1999).
19. Cutrale, F. et al. Hyperspectral phasor analysis enables multiplexed 5D in vivo imaging. *Nat. Methods* **14**, 149–152 (2017).
20. Scipioni, L., Rossetta, A., Tedeschi, G. & Gratton, E. Phasor S-FLIM: a new paradigm for fast and robust spectral fluorescence lifetime imaging. *Nat. Methods* **18**, 542–550 (2021).
21. Fereidouni, F., Bader, A. N. & Gerritsen, H. C. Spectral phasor analysis allows rapid and reliable unmixing of fluorescence microscopy spectral images. *Opt. Express* **20**, 12729 (2012).
22. Cutrale, F., Salih, A. & Gratton, E. Spectral phasor approach for fingerprinting of photo-activatable fluorescent proteins Dronpa, Kaede and KikGR. *Methods Appl. Fluoresc.* **1**, 35001 (2013).
23. von Chamier, L. et al. Democratising deep learning for microscopy with ZeroCostDL4Mic. *Nat. Commun.* **12**, 2276 (2021).
24. Weigert, M. et al. Content-aware image restoration: pushing the limits of fluorescence microscopy. *Nat. Methods* **15**, 1090–1097 (2018).
25. Stringer, C., Wang, T., Michaelos, M. & Pachitariu, M. Cellpose: a generalist algorithm for cellular segmentation. *Nat. Methods* **18**, 100–106 (2021).
26. Kolin, D. L. & Wiseman, P. W. Advances in image correlation spectroscopy: measuring number densities, aggregation states, and dynamics of fluorescently labeled macromolecules in cells. *Cell Biochem. Biophys.* **49**, 141–164 (2007).
27. Scipioni, L., Gratton, E., Diaspro, A. & Lanzanò, L. Phasor analysis of local ICS detects heterogeneity in size and number of intracellular vesicles. *Biophys. J.* **111**, 619–629 (2016).
28. Costantino, S., Comeau, J. W. D., Kolin, D. L. & Wiseman, P. W. Accuracy and dynamic range of spatial image correlation and cross-correlation spectroscopy. *Biophys. J.* **89**, 1251–1260 (2005).
29. Oneto, M. et al. Nanoscale distribution of nuclear sites by super-resolved image cross-correlation spectroscopy. *Biophys. J.* **117**, 2054–2065 (2019).
30. Petersen, N. O., Höddelius, P. L., Wiseman, P. W., Seger, O. & Magnusson, K. E. Quantitation of membrane receptor distributions by image correlation spectroscopy: concept and application. *Biophys. J.* **65**, 1135–1146 (1993).
31. Liang, Z., Lou, J., Scipioni, L., Gratton, E. & Hinde, E. Quantifying nuclear wide chromatin compaction by phasor analysis of histone Förster resonance energy transfer (FRET) in frequency domain fluorescence lifetime imaging microscopy (FLIM) data. *Data Brief* **30**, 105401 (2020).
32. Lou, J. et al. Phasor histone FLIM-FRET microscopy quantifies spatiotemporal rearrangement of chromatin architecture during the DNA damage response. *Proc. Natl Acad. Sci. USA* **116**, 7323–7332 (2019).
33. Wang, Y., Huang, H., Rudin, C. & Shaposhnik, Y. Understanding how dimension reduction tools work: an empirical approach to deciphering T-SNE, UMAP, TriMap, and PaCMAP for data visualization. *J. Mach. Learn. Res.* **22**, 1–73 (2021).
34. Fraley, C. & Raftery, A. E. Model-based clustering, discriminant analysis, and density estimation. *J. Am. Stat. Assoc.* **97**, 611–631 (2002).
35. Xiao, J., Lu, J. & Li, X. Davies Bouldin Index based hierarchical initialization K-means. *Intell. Data Anal.* **21**, 1327–1338 (2017).
36. Dickson, M. A. et al. Human keratinocytes that express hTERT and also bypass a p16(INK4a)-enforced mechanism that limits life span become immortal yet retain normal growth and differentiation characteristics. *Mol. Cell. Biol.* **20**, 1436–1447 (2000).
37. Tedeschi, G. et al. Monitoring macrophage polarization with gene expression reporters and bioluminescence phasor analysis. *Chem. Biomed. Imaging* **2**, 765–774 (2024).
38. Iriondo, O. et al. Distinct breast cancer stem/progenitor cell populations require either HIF1α or loss of PHD3 to expand under hypoxic conditions. *Oncotarget* **6**, 31721–31739 (2015).
39. Li, Q., Ma, R. & Zhang, M. $CoCl_2$ increases the expression of hypoxic markers HIF-1α, VEGF and CXCR4 in breast cancer MCF-7 cells. *Oncol. Lett.* **15**, 1119–1124 (2018).
40. Bai, F. et al. Simvastatin induces breast cancer cell death through oxidative stress up-regulating miR-140-5p. *Aging* **11**, 3198–3219 (2019).
41. Wang, R. et al. Molecular basis of V-ATPase inhibition by bafilomycin A1. *Nat. Commun.* **12**, 1782 (2021).
42. Dispersyn, G., Nuydens, R., Connors, R., Borgers, M. & Geerts, H. Bcl-2 protects against FCCP-induced apoptosis and mitochondrial membrane potential depolarization in PC12 cells. *Biochim. Biophys. Acta* **1428**, 357–371 (1999).
43. Sun, Y., Jiang, X., Chen, S. & Price, B. D. Inhibition of histone acetyltransferase activity by anacardic acid sensitizes tumor cells to ionizing radiation. *FEBS Lett.* **580**, 4353–4356 (2006).
44. Tóth, K. F. et al. Trichostatin A-induced histone acetylation causes decondensation of interphase chromatin. *J. Cell Sci.* **117**, 4277–4287 (2004).

45. Mylonis, I. et al. Hypoxia causes triglyceride accumulation by HIF-1-mediated stimulation of lipin 1 expression. *J. Cell Sci.* **125**, 3485–3493 (2012).
46. Munir, R., Lisec, J., Swinnen, J. V. & Zaidi, N. Lipid metabolism in cancer cells under metabolic stress. *Br. J. Cancer* **120**, 1090–1098 (2019).
47. Jones, S. P., Teshima, Y., Akao, M. & Marbán, E. Simvastatin attenuates oxidant-induced mitochondrial dysfunction in cardiac myocytes. *Circ. Res.* **93**, 697–699 (2003).
48. Zhang, Y. et al. Simvastatin improves lysosome function via enhancing lysosome biogenesis in endothelial cells. *Front. Biosci. Landmark Ed.* **25**, 283–298 (2020).
49. Liu, B., Zhu, F., Xia, X., Park, E. & Hu, Y. A tale of terminal differentiation: IKKα, the master keratinocyte regulator. *Cell Cycle* **8**, 527–531 (2009).
50. Monteleon, C. L. et al. Lysosomes support the degradation, signaling, and mitochondrial metabolism necessary for human epidermal differentiation. *J. Invest. Dermatol.* **138**, 1945–1954 (2018).
51. Gdula, M. R. et al. Remodeling of three-dimensional organization of the nucleus during terminal keratinocyte differentiation in the epidermis. *J. Invest. Dermatol.* **133**, 2191–2201 (2013).
52. Charest, J. L., Jennings, J. M., King, W. P., Kowalczyk, A. P. & García, A. J. Cadherin-mediated cell–cell contact regulates keratinocyte differentiation. *J. Invest. Dermatol.* **129**, 564–572 (2009).
53. Wynn, T. A., Chawla, A. & Pollard, J. W. Macrophage biology in development, homeostasis and disease. *Nature* **496**, 445–455 (2013).
54. Chen, S. et al. Macrophages in immunoregulation and therapeutics. *Signal Transduct. Target. Ther.* **8**, 207 (2023).
55. Xaus, J. et al. LPS induces apoptosis in macrophages mostly through the autocrine production of TNF-α. *Blood* **95**, 3823–3831 (2000).
56. Nayak, P., Bentivoglio, V., Varani, M. & Signore, A. Three-dimensional in vitro tumor spheroid models for evaluation of anticancer therapy: recent updates. *Cancers* **15**, 4846 (2023).
57. Ziperstein, M. J., Guzman, A. & Kaufman, L. J. Breast cancer cell line aggregate morphology does not predict invasive capacity. *PLoS One* **10**, e0139523 (2015).
58. Lee, S.-Y., Koo, I.-S., Hwang, H. J. & Lee, D. W. In vitro three-dimensional (3D) cell culture tools for spheroid and organoid models. *SLAS Discov.* **28**, 119–137 (2023).
59. Huang, Z., Yu, P. & Tang, J. Characterization of triple-negative breast cancer MDA-MB-231 cell spheroid model. *Onco Targets Ther.* **13**, 5395–5405 (2020).
60. Hofmann, S., Cohen-Harazi, R., Maizels, Y. & Koman, I. Patient-derived tumor spheroid cultures as a promising tool to assist personalized therapeutic decisions in breast cancer. *Transl. Cancer Res.* **11**, 134–147 (2022).
61. Gilazieva, Z., Ponomarev, A., Rutland, C., Rizvanov, A. & Solovyeva, V. Promising applications of tumor spheroids and organoids for personalized medicine. *Cancers* **12**, 2727 (2020).
62. Yao, Z. et al. Multiplexed bioluminescence microscopy via phasor analysis. *Nat. Methods* **19**, 893–898 (2022).
63. Tedeschi, G., Palomba, F., Scipioni, L. & Digman, M. A. Multimodal phasor approach to study breast cancer cell invasion in a 3D spheroid model. *Chem. Biomed. Imaging* **3**, 433–442 (2025).
64. Reynolds, D. S. et al. Breast cancer spheroids reveal a differential cancer stem cell response to chemotherapeutic treatment. *Sci. Rep.* **7**, 10382 (2017).
65. A. Naveena, H. & Bhatia, D. Hypoxia modulates cellular endocytic pathways and organelles with enhanced cell migration and 3D cell invasion. *Chembiochem* **24**, e202300506 (2023).
66. Bytautaite, M. & Petrikaite, V. Comparative study of lipophilic statin activity in 2D and 3D in vitro models of human breast cancer cell lines MDA-MB-231 and MCF-7. *Onco Targets Ther.* **13**, 13201–13209 (2020).
67. Held, M. et al. CellCognition: time-resolved phenotype annotation in high-throughput live cell imaging. *Nat. Methods* **7**, 747–754 (2010).
68. Viana, M. P. et al. Integrated intracellular organization and its variations in human iPS cells. *Nature* **613**, 345–354 (2023).
69. Kobayashi-Kirschvink, K. J. et al. Prediction of single-cell RNA expression profiles in live cells by Raman microscopy with Raman2RNA. *Nat. Biotechnol.* **42**, 1726–1734 (2024).
70. Wiggins, L. et al. The CellPhe toolkit for cell phenotyping using time-lapse imaging and pattern recognition. *Nat. Commun.* **14**, 1854 (2023).

Methods

The authors declare that this research complies with all relevant ethics regulations, under the University of California, Irvine biological use authorization (BUA) protocol BUA-R203.

Cell culture

All cell lines were obtained from ATCC, with the exception of N/TERT-2G keratinocytes[36] (a gift from J. P. H. Smits, Radboud University Medical Center, Nijmegen, The Netherlands). RAW264.7-NOS2 were obtained according to our previous work[37]. No authentication method was used.

RAW264.7-NOS2 cells and MDA-MB-231 cells were cultured in DMEM (DMEM high glucose, with L-glutamine, GenClone), supplemented with 10% v/v FBS (heat inactivated FBS, GenClone) and 1% v/v penicillin–streptomycin solution 100× (10,000 units of penicillin and 10 mg ml^{-1} streptomycin in 0.85% saline solution, GenClone). The RAW264.7-NOS2 cell line stably expresses the Nano-lantern CeNL under the *NOS2* promoter as described in our previous work[37], which consist of a luminophore (Nluc) linked to a fluorescent protein (mTurquoise2)[71]. MCF10A cells were cultured in DMEM/F12 medium (Gibco), supplemented with 5% v/v horse serum (heat inactivated, Invitrogen), epidermal growth factor (Peprotech), hydrocortisone (Sigma), cholera toxin (Sigma), insulin from bovine pancreas (Sigma), and 1% v/v penicillin–streptomycin solution 100× (10,000 units penicillin and 10 mg ml^{-1} streptomycin in 0.85% saline solution, GenClone). N/TERT-2G were cultured in Keratinocyte SFM (1X) medium (Gibco), supplemented with 50 µg ml^{-1} bovine pituitary extract (Gibco) and 5 ng ml^{-1} human recombinant EGF (Gibco) following the manufacturer instructions, and 1% v/v penicillin–streptomycin solution 100× (10,000 units penicillin and 10 mg ml^{-1} streptomycin in 0.85% saline solution, GenClone). All cell lines were cultured in a 37 °C and 5% CO_2 incubator

Labeling

LysoTrackerGreen DND-26 (ThermoFisher Scientific L7526), tetramethylrhodamine methyl ester (TMRM, Cayman Chemical 21437), SMCy5.5 (BioTechne 7295) and SiR-DNA (SiR-Hoechst, Cytoskeleton Inc.CY-SC007) were used throughout this work. A 1,000X mixture of these dyes (Lysotracker Green 200 µM, TMRM 100 µM, SMCy5.5 3 µM and SiR-Hoechst 670 µM) was prepared in dimethylsulfoxide and stored for a maximum of 4 weeks. The mixture was applied at 1X to cells upon plating, diluted with the culture medium, and at the moment of administering the treatments.

2D sample preparation

Cells were seeded in 8-well chambers (Cellvis) in the appropriate cell culture medium containing the 1X dye mixture. After 24 h half of the medium was replaced with the same medium containing the 1X dye mixture. MDA-MB-231, MCF10A and N/TERT-2G cells were seeded at 30,000 cells per well, RAW264.7-NOS2 cells were seeded at 50,000 cells per well.

Upon passaging, MCF10A cells were split into three flasks and passed in parallel for at least two additional passages, so that each flask constitutes a biological replicate. Each condition described below was tested on each of the replicates, with the exception of FCCP and bafilomycin A1, which were tested on a single replicate. For the stressor-exposure experiments, MCF10A cells were seeded in 8-well imaging chambers (Cellvis) at 30,000 cells per well in culture medium containing the 1X dyes mixture. The next day, the medium was replaced either with medium containing the 1X dyes mixture as the control or with medium containing the 1X dyes mixture + one of the following treatments, at the following final concentrations: anacardic acid (Sigma-Aldrich) 60 µM, trichostatin A (Sigma-Aldrich) 1 µM, bafilomycin A1 (Cayman Chemical) 50 nM, carbonyl cyanide-p-trifluoromethoxyphenylhydrazone (FCCP; Sigma-Aldrich) 1.25 µM, cobalt chloride $CoCl_2$ 400 µM (Sigma-Aldrich), simvastatin (Sigma-Aldrich) 20 µM. Cells were incubated for 24 h with the individual treatments before imaging.

For macrophage polarization experiments, RAW264.7-NOS2 cells were seeded at 50,000 cells per well in culture medium containing a 1X dyes mixture. The next day, half of the medium was replaced with medium containing the 1X dyes mixture as the control, and the other half was replaced with medium containing the 1X dyes mixture and LPS solution (Invitrogen) with a final concentration of 500 ng ml^{-1} for the polarization treatment.

For the keratinocyte calcium-switch experiments, N/TERT-2G cells were thawed and split into three flasks and passed in parallel for at least two passages, so that each flask constitutes a biological replicate. The control dataset was acquired on a single biological replicate in three technical replicates (multiple positions in the same well) while the calcium-induced differentiation was performed on all three biological replicates in three technical replicates (multiple positions in the same well). N/TERT-2G cells were seeded in 8-well imaging chambers (Cellvis) at 30,000 cells per well in culture medium containing the 1X dyes mixture. The next day, half of the medium was replaced with medium containing the 1X dyes mixture as the control, and the other half was replaced with medium containing the 1X dyes mixture and calcium chloride (Gibco) at a final concentration of 1.2 mM for the calcium-switch treatment. Upon thawing, N/TERT-2G cells were split into three flasks and passed in parallel for at least two passages, so that each flask constitutes a biological replicate. The control dataset was acquired on a single biological replicate in three technical replicates (multiple positions in the same well) while the calcium-induced differentiation was performed on all three biological replicates in three technical replicates (multiple positions in the same well).

Cell synchronization was performed according to the double thymidine block method. AU-565 cells (ATCC) were seeded in 8-well imaging chambers (Cellvis) at 7,000 cells per well in RPMI culture medium with L-glutamine (Dutscher L0500-500), supplemented with 1 mM sodium pyruvate and 10 mM HEPES (day 1). Two days later (day 3), the medium was changed to culture medium containing 2 mM thymidine and incubated for 18 h. On day 4, cells were washed three times in warm Dulbecco's phosphate-buffered saline (DPBS) and incubated in culture medium (without thymidine) for 9 h. On the evening of day 4, cells were incubated in culture medium with 2 mM thymidine and 1X ESPRESSO dye mixture for 16 h. On the morning of day 5, cells were washed three times in warm DPBS, incubated in medium containing 1x ESPRESSO dye mixture and imaged for 24 h with parameters listed in Supplementary Table 1, 5 min after medium change.

3D sample preparation

MDA-MB-231 spheroids were formed, starting from a culture of 10,000 cells per spheroid, mixed with the same medium used for 2D cell culture and a 2% v/v Cultrex UltiMatrix Reduced Growth Factor Basement Membrane Extract (BioTechne, R&D systems) solution in 96-well round-bottom plates (Corning Costar Ultra-Low Attachment Multiple Well Plate), similarly to our previous work[20,62]. After a brief centrifugation (5 min at 180 × *g*) and 24 h of incubation (37 °C, 5% CO_2), the spheroids were labeled with the dye mixture. The following day the spheroids were transferred to 8-well chambers (Cellvis) and embedded in a 2.0 mg ml^{-1} collagen type-1 gel matrix (Corning Collagen I, High concentration, Rat Tail, 100 mg). Medium containing the dye mixtures was added on top of the matrix after collagen polymerization and incubated at 37 °C and 5% CO_2 until the moment of imaging.

For the time lapse experiments, four different spheroids were prepared and imaged. For the data collected 72 h after embedding, four different spheroids per condition were prepared and imaged. At the moment of medium and dyes addition on top of the polymerized collagen matrix, the following compounds were added: simvastatin (Sigma-Aldrich) final concentration 20 µM; or cobalt chloride ($CoCl_2$, Sigma-Aldrich) final concentration 100 µM or 300 µM.

Viability assays and analysis

The number of viable cells was determined by quantifying the amount of ATP present (metabolically active cells) using the CellTiterGlo2 assay (Promega), following the manufacturer instructions. Cells were seeded in black, flat-bottom 96-well plates (Greiner Bio-One) and, 24 h later, Espresso-mix was added at a 1:1,000 ratio in the sample wells and not in the control wells. After 24 h the cells were washed and CellTiterGlo2 assay mix was added at a 2:1 ratio. Bioluminescence measurements were acquired with a Tecan Spark M10 multimode microplate reader. Three independent replicates were used.

Cells (N/TERT-2G, MDA-MB-231, RAW264.7-NOS2, MCF10A) were seeded in duplicate in 24-well plates. At 24 h, Espresso-mix was added at a 1:1,000 ratio in the sample wells and not in the control wells. At 24 h later, cells were washed, lifted and counted using a Countess II Automated Cell Counter (ThermoFisher). The total number of cells and number of live cells were recorded.

Graphs were generated and statistical analysis (multiple t-test, unpaired, non-parametric, Kolmogorov–Smirnov test, threshold for *P* value set at 0.05, Holm–Sidak method for correction of multiple comparisons) was carried out using Graphpad PRISM (v10.3.0).

Hyperspectral imaging and unmixing

Imaging was performed with a Zeiss LSM880 with Spectral (Quasar) detector and ZEN 2.3 Black software for acquisition (v14.0.29.201). ESPRESSO images were acquired with a ×63, 1.4 numerical aperture (NA) oil objective (Zeiss) with a variable number of tiles, each tile consisting of a 512 × 512 pixels image with a 120 nm pixel size, and spheroid measurements were acquired with a ×40/0.75 NA air objective (Zeiss). Two dichroic mirrors (MBS 488/561/633 and MBS 405) were selected for excitation with 488, 561, 633 and/or 405 nm lasers. All measurements in 2D were taken with both the 488 nm (0.1%, corresponding to 0.2 µW) and the 633 nm (1%, corresponding to 4 µW) lasers, and macrophage polarization measurements also include excitation with the 405 nm laser (0.2%, corresponding to 5.5 µW) for the gene expression reporter. All measurements in spheroids were taken with both the 488 nm (0.5%, corresponding to 6.9 µW) and the 633 nm (1.5%, corresponding to 7.7 µW) lasers. Laser power was measured after the objective using a power meter set for each specific wavelength (Thorlabs). Images are saved as Zeiss.lsm files. For spectral unmixing, average emission spectra from MDA-MB-231 cells labeled with the individual dyes have been imaged and saved in a database. During processing, the spectra are loaded and transformed in spectral coordinates (up to the second harmonic, enabling up to five-color unmixing) and used as pure components for linear unmixing. Negative values in the unmixed images are set to 0. The raw (.lsm) images after unmixing are saved as .npy files.

CARE denoising training

The CARE network has been trained on a total of 128 noisy and 128 high signal-to-noise ratio 512 × 512 pixels images of MDA-MB-231 and MCF10A cells. Images were acquired sequentially, with the noisy image acquired first and the second acquired with the same parameters but with 16x line averaging (during scanning, each line of the image is scanned 16 times and the average intensity is then displayed) for higher signal-to-noise ratio. For each image, the mean intensity of the high signal-to-noise ratio image was scaled to the mean intensity of the corresponding low signal-to-noise ratio image, and Poisson noise is artificially added to degrade it. The degraded high signal-to-noise ratio image is used for training because the organelles are in the same position as in the non-degraded high signal-to-noise ratio image that is used as the ground truth. Each image is spectrally unmixed by phasor, and each unmixed channel (lysosomes, mitochondria, lipid droplets and DNA) is trained separately. Training is performed on 64 × 64 pixels patches, of which only the 50% brightest were considered. The data are then split 80/20 into training/validation, and the CARE network is trained with a kernel size of 3 and a batch size of 8 for 250 epochs for each channel. The CARE network and the training parameters are saved in a dictionary that is used as an input in the ESPRESSO pipeline.

Image processing parameters

Single-cell segmentation is performed with CellPose (v2.2.2) using the pre-trained network cyto2. Input images are 2-channel images consisting of the SiR-Hoechst channel (nucleus) and the sum of the other organelle channels (cytoplasm) binned 2 × 2 (every 2 × 2 group of pixels is averaged to obtaine one single pixel value), normalized to the 99th percentile and converted in uint8. Different diameters (in pixels) are entered for the different cell types (MDA-MB-231 (2D), N/TERT-2G and MCF10A, 175; RAW246.7-NOS2, 125; MDA-MB-231 (3D), 30).

Feature extraction

Once segmented, the organelle images for each cell are analyzed as follows. For each individual channel, the intensity distribution is calculated over 512 logarithmic bins ranging from 10^{-2} to 10^{3} and normalized so that its sum equals 1, and the ICS auto-correlation function is calculated. For each ICS auto-correlation function, the rotational average is obtained and padded with zeros to 128 pixels. For each channel combination, the ICCS image cross-correlation function is computed and analyzed in the same way as ICS. Each bin of these functions (intensity histograms, ICS and ICCS functions) are passed as features for the next analysis step, yielding a total of 3,328 features (512 each for the four intensity histograms, 128 each for the four auto-correlation functions and another 128 each for the six cross-correlation functions). A Pandas DataFrame of the same length of the number of segmented cells is compiled and the organelle features are stored along with the position of the cells in the image (calculated as the center of mass of the CellPose mask), the name of the file and the ID of the cell.

Feature selection

For data analysis, multiple files are entered into the same pipeline (for example, experimental replicates, control and treatment conditions, multiple timepoints…), are identified based on their file name and a name is assigned to each file depending on the condition to which it refers. Additionally, the conditions for which to perform the feature comparison are chosen. For static experiments, all conditions are considered, while for dynamics experiments only the final time point is used for feature selection. For every feature for each pair of conditions considered for feature comparison, a Kolmogorov–Smirnov test with Bonferroni correction for multiple comparisons is performed and the *P* value is stored along with the difference between the median value across all cells for each feature. A scatterplot (analog to the volcano plot for scRNA-seq) of $-\log_{10}(P \text{ value})$ as a function of the difference of the medians is drawn for functional (intensity histograms) and morphological (ICS and ICCS functions) features, and the user then defines a range of *P* values and median differences to use for dimensionality reduction. A subset of the organelle profile including only the selected features is used for dimensionality reduction.

PaCMAP and clustering

PaCMAP dimensionality reduction is performed using the Python library pacmap (v0.7.0), outputting three dimensions and selecting random_state = 1. Only the conditions used for the feature selection are used to define the space, and the cells associated with the remaining conditions are projected into that space. At this stage, a Gaussian mixture model clustering step is performed with a varying number of clusters (from 2 to 16) and of initial states (from 0 to 100 in steps of 10) to calculate the Davies–Bouldin index for each condition. After testing all conditions, the Davies–Bouldin index is plotted as a function of the number of clusters; the number of clusters and of initial states are user-defined based on the minima of the curves and the degree of detail required by the clustering.

Data visualization
ESPRESSO PaCMAPs are saved for all three dimensions as scatter plots, in which each point is color-coded according to either their experimental conditions or their associated cluster, together with bar plots of the absolute or normalized contribution of each condition or cluster. The center of mass for the organelle functions (intensity histograms, ICS and ICCS functions) is also calculated and used to color-code the ESPRESSO PaCMAPs for a visual representation of the organelle properties. Finally, the segmentation masks are loaded and the mask corresponding to each cell is color-coded based on its associated cluster. For time-resolved experiments, the output is a GIF of the color-coded masks and the corresponding PaCMAP, evolving as a function of time.

Spatial analysis
Spatial analysis was performed using SquidPy[72]. ESPRESSO localizations and cluster numbers were converted into annotated data. Spatial statistics were calculated and analyzed using the spatial_neighbors and nhood_enrichment functions to ultimately obtain the neighborhood enrichment z-scores.

Temporal analysis
Cell tracking was performed using TrackPy (https://soft-matter.github.io/trackpy/v0.6.4/, v0.6.1). For each cell, a Pandas DataFrame containing the organelle features is computed, including the spatial position of the cell (calculated as the centroid of the CellPose masks outputted from the segmentation step), and the frame at which the cell was detected. The DataFrame is passed to TrackPy, using a search range of 50 pixels, memory of 1, adaptive stop of 1 and adaptive step of 0.95. TrackPy analysis outputs a DataFrame in which the (x,y,t) positions of each cell are linked via a particle identifier. To construct the cell state transition maps, a 2D N x N matrix is constructed, with N being the total number of clusters, and the number of tracks starting from cluster i and ending in cluster j is shown in position (i,j), with i,j = 1, …, N.

Single-cell library preparation and sequencing for scRNA-seq
Single-cell 3′ RNA-seq experiments were conducted using the Chromium single cell system (10x Genomics) and the NovaSeq 6000 sequencer (Illumina). The concentration of the single-cell suspension was counted using Countess 3 (Thermo) and adjusted to 1,200 cells μl^{-1}. The cell libraries were generated using the standard manufacturer's protocol (Chromium Single Cell 3′ Reagent Kits v3). The resulting libraries were pooled and sequenced using 28 bp plus 90 bp paired-end reads on the Illumina NovaSeq 6000 system, targeting a read depth of 50,000 reads per cell.

Single-cell data processing and analysis for scRNA-seq
The CellRanger Pipeline (v7.1.0) was used to align reads and generate count matrices against the human genome (GRCh38-2020-A, obtained from 10x Genomics). For downstream analysis of the data we used the Seurat (v4.3.0) R package to combine all cell libraries, and a merged Seurat object was generated. Genes detected in <3 cells were removed. Low-quality cells were further filtered based on sample-specific quality control metrics, with different thresholds applied to individual samples: in the control sample, cells with >2,000 and <15,000 detected genes per cell, >5,000 and <125,000 UMIs (unique molecular identifiers) per cell and <2% mitochondrial gene expression were retained; and in the calcium-induced sample, cells with >2,500 and <10,000 detected genes per cell, >5,000 and <125,000 UMIs per cell and <2% mitochondrial gene expression were included in the analysis.

In addition, the EmptyDrops algorithm[73] was applied to each sample to identify and annotate empty droplets. The predicted empty cells were further validated using the FeaturePlot() function, assessing metrics such as nFeature_RNA, nCount_RNA, percent.mt and Empty_Droplet. Clusters enriched with empty droplets were subsequently excluded from the dataset. To identify potential doublets, we used DoubletFinder(v2.0)[74] and scDblFinder(v1.18.0)[75]. Doublets predicted by both algorithms and annotated as 'doublet:Doublet' were selectively removed to ensure accurate results while preserving as many cells as possible. Only a small number of doublets were detected in the dataset, and no doublet-specific clusters were predicted by either algorithm. The combination of these filtering steps yielded a final dataset comprising 11,907 high-quality single-cell transcriptomes.

To address inter-individual differences and potential batch effects, the merged Seurat object was normalized using the NormalizeData() function with a scale factor of 10,000, and variable features were identified using FindVariableFeatures() with 2,000 genes. Principal component analysis (PCA) was then performed, and the first 30 principal components (PCs) were used for uniform manifold approximation and projection (UMAP) dimensionality reduction. Clustering was conducted using the FindNeighbors() and FindClusters() functions with 30 PCA components and a resolution parameter set to 0.5. To evaluate inter-individual differences, a library-split UMAP plot was generated using the DimPlot() function. Batch effects across different libraries were assessed using the distribution of PC_1 and PC_2 from the PCAs (Supplementary Fig. 10f). Calcium-specific cells were identified in the merged Seurat object. To determine whether this batch-to-batch variation required correction, CytoTRACE (v.0.3.3)[76] was used with default parameters to compare cellular differentiation states between N/TERT-2G keratinocytes in the dataset. The observed overlap between calcium-specific cells and higher differentiation scores suggests that biological differences, rather than technical variation, are the primary drivers of heterogeneity in the data (Supplementary Fig. 10f,g).

Cluster markers were interpreted and cluster identities were assigned based on known cell type annotations from Enzo et al.[77]. These markers were further used to classify cells into holoclone (H), meroclone (M) or paraclone (P) states. To evaluate the stress response in our dataset, we analyzed stress response-related genes previously reported[77], including *CREBRF, DDIT3, XBP1, MAFF*, *PPP1R15A* and *HSPB8*. To further assess the overall stress levels in the samples, *KRT14* and three housekeeping genes (*ACTB*, *GAPDH* and *RPS18*) were used as positive controls (Supplementary Fig. 2d,e).

Functional gene set enrichment analysis for scRNA-seq
To integrate organelle dye-based features with gene-based scRNA-seq data, we transformed the gene expression data into function-based gene set enrichment scores using single-sample gene set enrichment analysis, as implemented in the escape R package[78]. This transformation replaced the gene count matrix with a single-cell function enrichment matrix, incorporating four assay categories: GO_CC, GO_BP, GO_MF and Hallmarks. The gene sets related to lysosomal acidity, chromatin organization and mitochondrial function were sourced from the Molecular Signature Database (MsigDB, http://software.broadinstitute.org/gsea/msigdb/).

Statistics and Reproducibility
No statistical method was used to predetermine the sample size. No data were excluded from the analyses, with the exception of the ESPRESSO-specific cluster in Figure 6, as described and discussed above.

Reporting summary
Further information on research design is available in the Nature Portfolio Reporting Summary linked to this article.

Data availability
Demonstration data are available from Zenodo: https://zenodo.org/records/12737891 (ref. 79). Due to data size constraints, imaging data can be requested from Lorenzo Scipioni (lorenzo.scipioni@inserm.fr).

Code availability

Demonstration code is available from Zenodo: https://zenodo.org/records/12737891, scRNA-seq analysis can be found at https://github.com/yl-jia/ESPRESSO.

References

71. Suzuki, K. et al. Five colour variants of bright luminescent protein for real-time multicolour bioimaging. *Nat. Commun.* **7**, 13718 (2016).
72. Palla, G. et al. Squidpy: a scalable framework for spatial omics analysis. *Nat. Methods* **19**, 171–178 (2022).
73. Lun, A. T. L. et al. EmptyDrops: distinguishing cells from empty droplets in droplet-based single-cell RNA sequencing data. *Genome Biol.* **20**, 63 (2019).
74. McGinnis, C. S., Murrow, L. M. & Gartner, Z. J. DoubletFinder: doublet detection in single-cell RNA sequencing data using artificial nearest neighbors. *Cell Syst.* **8**, 329–337 (2019).
75. Germain, P.-L., Lun, A., Meixide, C. G., Macnair, W. & Robinson, M. D. Doublet identification in single-cell sequencing data using *scDblFinder*. *F1000Res* **10**, 979 (2022).
76. Gulati, G. S. et al. Single-cell transcriptional diversity is a hallmark of developmental potential. *Science* **367**, 405–411 (2020).
77. Enzo, E. et al. Single-keratinocyte transcriptomic analyses identify different clonal types and proliferative potential mediated by FOXM1 in human epidermal stem cells. *Nat. Commun.* **12**, 2505 (2021).
78. Borcherding, N. et al. Mapping the immune environment in clear cell renal carcinoma by single-cell genomics. *Commun. Biol.* **4**, 122 (2021).
79. Scipioni, L. Demo code for 'ESPRESSO: spatiotemporal omics based on organelle phenotyping': https://doi.org/10.1101/2024.06.13.598932. *Zenodo* (2024).

Acknowledgements

This work was supported by funds from the Fondation Toulouse Cancer Santé (Chaire Oncobreast to L.S.), the National Science Foundation grants CBET2134916 to S.X.A. and Y.Y.J. and 1847005 to M.A.D., and the Allen Distinguished Investigator Award, a Paul G. Allen Frontiers Group advised grant of the Paul G. Allen Family Foundation (to J.A.P. and M.A.D.). The authors acknowledge the support of the Laboratory for Fluorescence Dynamics (P41GM103540), the American Italian Cancer Foundation (to M.D.B.), the Chao Family Comprehensive Cancer Center Genomics High-Throughput Facility Shared Resource, supported by the NCI of the NIH under award no. P30CA062203, and the UCI Skin Biology Resource Center supported by NIAMS under award no. P30AR075047.

Author contributions

L.S. conceived the idea, performed experiments and wrote code. G.T. conceived the idea and performed experiments. M.X.N. generated the RAW246.7-NOS2 cell line. Y.Y.J. performed and analyzed the scRNA-seq experiments. Y.Y.J. and S.X.A. advised on the keratinocytes experiments and interpretation. S.Z. performed the cell cycle experiment. L.P.H. performed the viability assays. M.D.B. provided reagents and helped with interpretation. S.X.A., J.A.P., E.G. and M.A.D. provided support and supervised the project. L.S. took the lead in writing the manuscript. All authors provided critical feedback and helped shape the research, analysis and manuscript.

Competing interests

The authors declare no competing interests.

Additional information

Supplementary information The online version contains supplementary material available at https://doi.org/10.1038/s41592-025-02863-4.

Correspondence and requests for materials should be addressed to Lorenzo Scipioni or Michelle A. Digman.

Peer review information *Nature Methods* thanks Sang-Hee Shim and the other, anonymous, reviewer(s) for their contribution to the peer review of this work. Primary Handling Editor: Madhura Mukhopadhyay, in collaboration with the *Nature Methods* team.

nature portfolio

Corresponding author(s): Lorenzo Scipioni, Michelle Digman

Last updated by author(s): Jul 5, 2025

Reporting Summary

Nature Portfolio wishes to improve the reproducibility of the work that we publish. This form provides structure for consistency and transparency in reporting. For further information on Nature Portfolio policies, see our Editorial Policies and the Editorial Policy Checklist.

Statistics

For all statistical analyses, confirm that the following items are present in the figure legend, table legend, main text, or Methods section.

n/a	Confirmed
☐	☒ The exact sample size (*n*) for each experimental group/condition, given as a discrete number and unit of measurement
☐	☒ A statement on whether measurements were taken from distinct samples or whether the same sample was measured repeatedly
☐	☒ The statistical test(s) used AND whether they are one- or two-sided *Only common tests should be described solely by name; describe more complex techniques in the Methods section.*
☐	☒ A description of all covariates tested
☐	☒ A description of any assumptions or corrections, such as tests of normality and adjustment for multiple comparisons
☐	☒ A full description of the statistical parameters including central tendency (e.g. means) or other basic estimates (e.g. regression coefficient) AND variation (e.g. standard deviation) or associated estimates of uncertainty (e.g. confidence intervals)
☐	☒ For null hypothesis testing, the test statistic (e.g. *F*, *t*, *r*) with confidence intervals, effect sizes, degrees of freedom and *P* value noted *Give P values as exact values whenever suitable.*
☒	☐ For Bayesian analysis, information on the choice of priors and Markov chain Monte Carlo settings
☒	☐ For hierarchical and complex designs, identification of the appropriate level for tests and full reporting of outcomes
☒	☐ Estimates of effect sizes (e.g. Cohen's *d*, Pearson's *r*), indicating how they were calculated

Our web collection on statistics for biologists contains articles on many of the points above.

Software and code

Policy information about availability of computer code

Data collection	Data were collected using the ZEN 2.3 Black software for acquisition (version 14.0.29.201).
Data analysis	Data analysis was performed in Python (environment information provided at https://zenodo.org/records/12737891), statistical analysis was performed in Python and GraphPad PRISM (Version 10.3.0)

For manuscripts utilizing custom algorithms or software that are central to the research but not yet described in published literature, software must be made available to editors and reviewers. We strongly encourage code deposition in a community repository (e.g. GitHub). See the Nature Portfolio guidelines for submitting code & software for further information.

Data

Policy information about availability of data

All manuscripts must include a data availability statement. This statement should provide the following information, where applicable:

- Accession codes, unique identifiers, or web links for publicly available datasets
- A description of any restrictions on data availability
- For clinical datasets or third party data, please ensure that the statement adheres to our policy

Demo data are available from Zenodo: https://zenodo.org/records/1273789179, other data can be requested from Lorenzo Scipioni (lorenzo.scipioni@inserm.fr)

Research involving human participants, their data, or biological material

Policy information about studies with human participants or human data. See also policy information about sex, gender (identity/presentation), and sexual orientation and race, ethnicity and racism.

Reporting on sex and gender	N/A
Reporting on race, ethnicity, or other socially relevant groupings	N/A
Population characteristics	N/A
Recruitment	N/A
Ethics oversight	N/A

Note that full information on the approval of the study protocol must also be provided in the manuscript.

Field-specific reporting

Please select the one below that is the best fit for your research. If you are not sure, read the appropriate sections before making your selection.

☒ Life sciences ☐ Behavioural & social sciences ☐ Ecological, evolutionary & environmental sciences

For a reference copy of the document with all sections, see nature.com/documents/nr-reporting-summary-flat.pdf

Life sciences study design

All studies must disclose on these points even when the disclosure is negative.

Sample size	Not estimated as each replicate is comprised by hundreds to several thousands cells
Data exclusions	No point was excluded, except in Figure 5, where one cluster specific to ESPRESSO phenotyping was excluded in the comparison with scRNA-seq, as described in the main text
Replication	Information about replication is included in the main text
Randomization	Not relevant, experimental conditions did not require grouping
Blinding	Not relevant, experimental conditions did not require grouping

Reporting for specific materials, systems and methods

We require information from authors about some types of materials, experimental systems and methods used in many studies. Here, indicate whether each material, system or method listed is relevant to your study. If you are not sure if a list item applies to your research, read the appropriate section before selecting a response.

Materials & experimental systems

n/a	Involved in the study
☒	☐ Antibodies
☐	☒ Eukaryotic cell lines
☒	☐ Palaeontology and archaeology
☒	☐ Animals and other organisms
☒	☐ Clinical data
☒	☐ Dual use research of concern
☒	☐ Plants

Methods

n/a	Involved in the study
☒	☐ ChIP-seq
☒	☐ Flow cytometry
☒	☐ MRI-based neuroimaging

Eukaryotic cell lines

Policy information about cell lines and Sex and Gender in Research

Cell line source(s)	MCF10A and MDA-MB-231 were obtained from ATCC, with the exception of N/TERT-2G keratinocytes36 (a gift from Jos P. H.

Cell line source(s)	Smits, Radboud University Medical Center, Nijmegen, The Netherlands). RAW264.7-NOS2 were obtained according to our previous work.
Authentication	Cell lines were not authenticated
Mycoplasma contamination	All cells tested negative for mycoplasma
Commonly misidentified lines (See ICLAC register)	No commonly misidentified cell lines were used in this study

Plants

Seed stocks	N/A
Novel plant genotypes	N/A
Authentication	N/A